Atomic insights into the competitive edge of nanosheets splitting water

Lorenz J. Falling[1,2]*, Woosun Jang[1,3], Sourav Laha[4,5], Thomas Götsch[1], Maxwell Terban[5], Rik Mom[1,6], Juan-Jesús Velasco-Vélez[1,7], Frank Girgsdies[1], Detre Teschner[1], Andrey Tarasov[1], Cheng-Hao Chuang[8], Thomas Lunkenbein[1], Axel Knop-Gericke[1], Daniel Weber[5,10], Robert Dinnebier[5], Bettina V. Lotsch[5], Robert Schlögl[1], Travis E. Jones[1,7]*

1 Fritz Haber Institute of the Max Planck Society, Berlin 14195, Germany

2 School of Natural Sciences, Technical University Munich, 85748 Munich

3 Integrated Science & Engineering Division, Underwood International College, Yonsei University, Incheon 21983, Republic of Korea

4 Department of Chemistry, National Institute of Technology Durgapur, Mahatma Gandhi Avenue, West Bengal-713209, India

5 Max Planck Institute for Solid State Research, Stuttgart 70569, Germany

6 Leiden Institute of Chemistry, Leiden University, 2300 RA Leiden, The Netherlands

7 Experiments division, ALBA Synchrotron Light Source, Cerdanyola del Vallés, Barcelona 08290, Spain.

8 Department of Physics, Tamkang University, Tamsui 251, Taiwan

9 Wallenberg Initiative Materials Science for Sustainability, Chemistry and Chemical Engineering, Chalmers University of Technology, 41296 Gothenburg, Sweden

10 Theoretical Division, Los Alamos National Laboratory, Los Alamos, NM 87545

* To whom correspondence should be addressed: lorenz.falling@tum.de and tejones@lanl.gov

Abstract

The oxygen evolution reaction (OER) provides the protons for many electrocatalytic power-to-X processes, such as the production of green hydrogen from water or methanol from CO_2. Iridium oxo-hydroxides (IOHs) are outstanding catalysts for this reaction because they strike a unique balance between activity and stability in acidic electrolytes. Within IOHs, this balance varies with atomic structure. While amorphous IOHs perform best, they are least stable. The opposite is true for their crystalline counterparts. These rules-of-thumb are used to reduce the loading of scarce IOH catalysts and retain performance. However, it is not fully understood how activity and stability are related on the atomic level, hampering rational design. Herein, we provide simple design-rules (Figure 12) derived from literature and various IOHs within this study. We chose crystalline IrOOH nanosheets as our lead material because they provide excellent catalyst utilization and a predictable structure. We found that nanosheets combine the chemical stability of crystalline IOHs with the activity amorphous IOHs. Their dense bonding network of pyramidal trivalent oxygens ($\mu_{3\Delta}$–O) provides structural integrity, while allowing reversible reduction to an electronically gapped state that diminishes the destructive effect of reductive potentials. The reactivity originates from coordinative unsaturated edge sites with radical character, i.e. μ_1–O oxyls. By comparing to other IOHs and literature, we generalized our findings and synthesized a set of simple rules that allow prediction of stability and reactivity of IOHs from atomistic models. We hope that these rules will inspire atomic design strategies for future OER catalysts.

Keywords

Introduction

Proton exchange membrane (PEM) electrolyzers can produce green hydrogen dynamically at high purity and pressure.[1–3] These benefits make them increasingly popular to produce green hydrogen on demand, but PEM electrolyzers cannot fuel a hydrogen economy of scale because of scarce catalyst materials for the oxygen evolution reaction (OER) – one half-reaction of water electrolysis. The state-of-the-art OER catalyst with the best balance of stability and activity are iridium oxo-hydroxides (IOHs), which make them an interesting model for the development of more abundant catalyst materials, or – at high metal utilization [4] – promising candidates for devices with high-end performance.

Among IOHs, amorphous IOHs are particularly active.[5–8] In contrast to their crystalline counterparts, amorphous IOHs are hydrated [9–12] and exhibit large surface areas,[5,13,14] leading to a lower Ir–O connectivity and lower oxidation states in ambient conditions – typically between Ir^{III} and Ir^{IV}.[6,7,15] Interestingly, the higher activity of amorphous IOHs cannot not be fully explained by their larger surface area. Instead, amorphous IOHs are intrinsically more active than their crystalline counterparts.[5,6,13,14,16] On the downside, they are more prone to transient dissolution during oxidation and reduction.[17–20] This suggest that lower Ir–O connectivity causes higher intrinsic activities at the cost of stability for noble metal catalysts. However, the correlation is not straightforward. For IOH films calcined between 100 and 600 °C, Geiger et al. found an optimum balance of activity and stability between 400 and 500 °C.[18] Their findings show that stability and activity are correlated, but in a complex way.

Pinpointing which atomic connectivity in amorphous IOHs leads to an optimum balance of activity and stability is not trivial. The problem can be separated in two parts. First, the role of Ir–O species under operating conditions needs to be known, and second, connected to the distribution of Ir–O species, i.e. the connectivity.

The first part has been addressed, among other techniques,[21,22] by X-ray spectroscopy. X-ray spectroscopy is a tool well suited to study the role of Ir–O species on IOH surfaces, due to their surface sensitivity when using soft X-rays and distinct signals from different Ir–O species.[20,23–26] In an effort to utilize this spectroscopy under wet conditions, a variety of in situ approaches have been developed [27,28] and used on iridium dioxide,[29,30] anodized metallic iridium thin films [30,31] and nanoparticles,[25,32,33] amorphous IOHs with varying pre-treatment,[20] and mesoporous IOH films.[34] By comparing to calculated spectroscopy of a rutile-type IrO_2 model system, these studies were able to identify electron deficient oxygen species that are reactive.[25,30–32] This negative charge transfer behavior between Ir and O occurs when iridium is oxidized beyond Ir^{IV}.[32,33,35] The dynamic behavior of the electron deficient oxygen

species under applied bias was further used to connect Ir–O species to electrochemical oxidation events [20,25] and their impact on the reaction barrier of the rate determining step in the OER employing ab initio molecular dynamics. [36]

The preliminary consensus on Ir–O speciation in the above studies is that surface oxygens bound to one iridium atom (μ_1–O) are oxyls when stripped of all protons and are the most active species, oxygens bound to two iridium atom (μ_2–O) contribute to a larger surface electron hole density and serve as proton-acceptors in the rate determining O-O coupling step, and the remaining μ_3–O species contribute to stability through connectivity.

In this work, we use this knowledge about Ir–O species and their properties and expand it to the distribution of μ_x–O species, i.e. the Ir–O connectivity. To that end we use crystalline IrOOH nanosheets that have a predictable connectivity, such as rutile-type IrO_2, and have a hydrated structure, such as amorphous IOHs. [37–39] This hybrid behavior makes IrOOH a suitable model system to explain the relationships between connectivity, activity, and stability for crystalline and amporphous IOHs alike.

Apart from being an interesting model system, IrOOH nanosheets are promising for real world application. They have been reported to be more active than amorphous IOHs, [37–39] relatively stable, [37,39] and utilize iridium more effectively than nanoparticles. [37] These properties combined make IrOOH nanosheets an interesting candidate to lower iridium utilization below 0.01 g_{Ir}/kW, a critical limit for large-scale application of PEM electrolyzers. [40]

Our work describes all steps necessary to get from the material IrOOH to a set of qualitative rules about the relationship between connectivity, activity, and stability that apply to most IOHs. It starts with a characterization of the crystal structure of bulk and nanosheet IrOOH. Based on the experimental structure, we predict the electrochemical behavior of IrOOH with ab-initio methods. We then test the predictions with operando X-ray spectroscopy. This interplay between model and experiment allows us to uncover a relationship of connectivity and function. To generalize the findings, we qualitatively compare IrOOH against the operando scpectroscopy of other well-studied IOHs. The result of this comparison is synthesized into a "cheat-sheet" on how connectivity relates to the function of IOHs.

Results

Bulk IrOOH is synthesized from a precursor material $K_{0.75}Na_{0.25}IrO_2$ by exchanging the cations for protons in 1 M HCl. IrOOH are dark crystallites with a tinge of pink. Exfoliation to nanosheets was done using tetrabutyl ammonium hydroxide (TBAOH), ultrasonication, and centrifugation. For more information on synthesis, please visit the experimental section and supporting information (SI).

IrOOH crystal structure

The powder X-ray diffraction (PXRD) pattern of the synthesized IrOOH shown in Figure 1A exhibits sharp hk0 reflections demonstrating well-ordered heterogenite type sheets, and significant broadening of the 00l series indicating smaller domain size or stacking disorder (see SI for full discussion). In addition to the brucite-1T type pattern, we observe superstructure reflections at ~35° and ~44° 2θ (inset of Figure 1A), which can be indexed successfully by AB stacking, i.e. a heterogenite-2H type model (space group $P6_3/cmm$. ABC stacking could be ruled out (see SI). Further support for the heterogenite-2H structure comes from density functional theory (DFT) calculations, which predicts the formation energy per atom in heterogenite-2H to be 0.26 eV lower than that in brucite IrOOH (see Table S2).

The heterogenite-2H structure from PXRD was used as a starting point to analyze the pair distribution function (PDF) of IrOOH (Figure 1B). The observed and simulated oscillations of the PDF match well in the local structure range up to 15 Å, indicating good short- to medium-range order (see SI for more detail). The average Ir-O distance was found to be 2.01 Å and the closest Ir-Ir distance 3.11 Å. These distances are close to what was observed by PXRD, namely 2.05 Å and 3.10 Å, respectively. DFT calculations of fully relaxed heterogenite-2H structures found 2.10 Å for the average Ir-O bond length and 3.23 Å for the closest Ir-Ir distance.
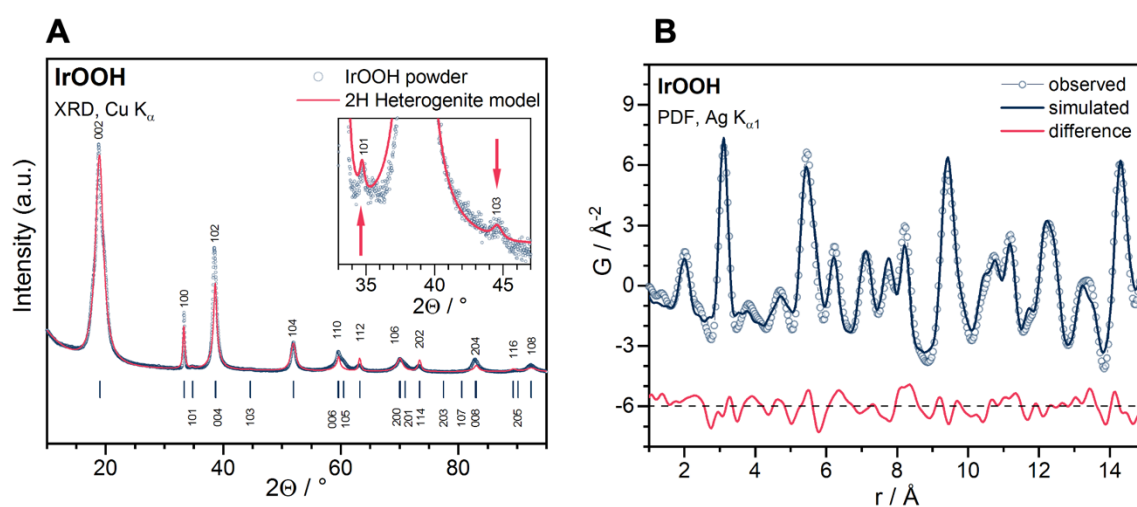

Figure 1: Structural characterization of IrOOH; **A** Diffractogram (blue symbols) and Rietveld simulation (red line) of the heterogenite-2H with an AB-stacking, Laue indices of intense reflections are given above the curve; the inset shows the two superstructure reflections at 35° and 45° (marked with red arrows); **B** the simulated (dark blue line) and observed (light blue line and symbols) pair distribution function obtained from a heterogenite-2H model and IrOOH X-ray scattering, respectively; the difference is shown in red with an offset of -6.

The crystal structure of IrOOH nanosheets on a graphene substrate graphene (see experimental details for transfer method) have been characterized on a gold grid (see Figure 2) with selected area electron diffraction (SAED) in a transmission electron microscope (TEM). The crystallites are partly stacked, but single sheets can still be seen clearly (Figure 2A). Selected area electron diffraction (Figure 2D) shows diffraction patterns of graphene and one IrOOH nanosheet. The latter agree with a calculated pattern of heterogenite-2H (Figure 2F), which resulted in an Ir–Ir distance of 3.15 Å ($\approx$ 3.11 Å from PXRD). 50 cyclovoltagrams (CVs) between 0.35 and 1.65 V_{RHE} do not alter the structure significantly (see Figure 2B&E and Table S7).
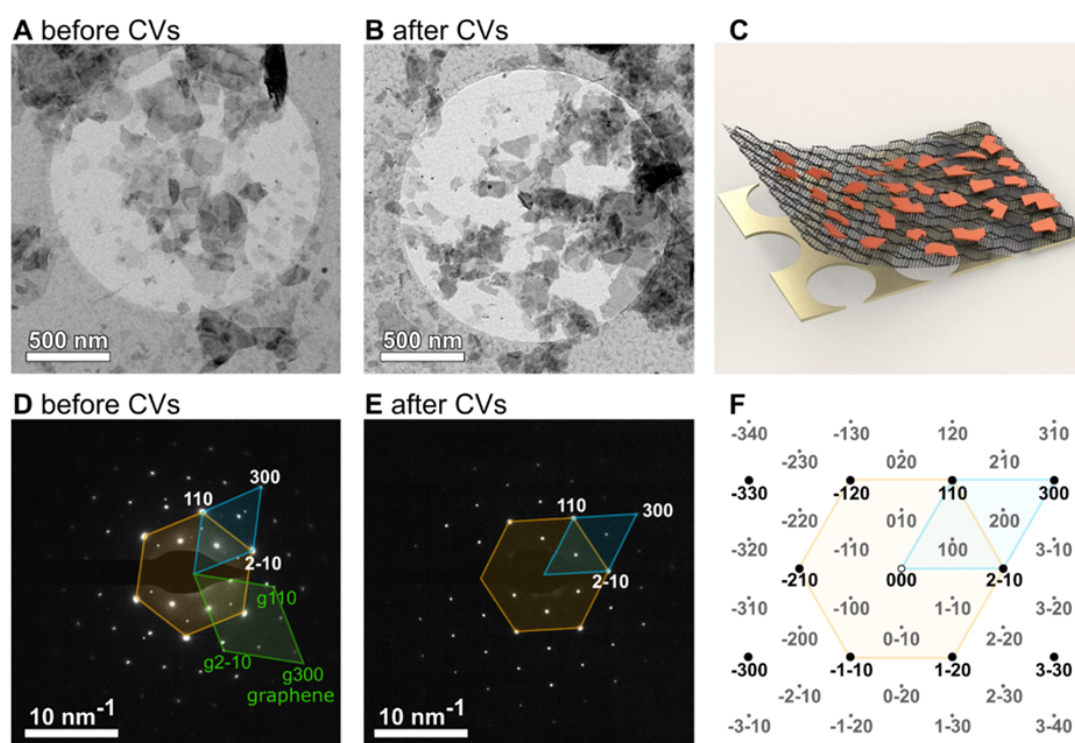

Figure 2: Transmission Electron Microscope (TEM) bright field micrograph **A** before and **B** after 50 CVs between 0.35 and 1.6 V_{RHE}; the respective electron diffractograms of a single sheet are shown in **D** and **E**, in which polygons represent the conventional (orange) and primitive (blue) reciprocal unit cells of IrOOH nanosheets or graphene (green); **F** calculated map of reflection spots for the diffractograms; **C** artistic rendering of the TEM samples with a single layer of graphene (dark grey), nanosheets (red) on a holey TEM gold grid (beige).

Electronic structure and hydrogen defects

The atomic positions of iridium and oxygen have a direct impact on the electronic structure of IrOOH and thereby their electrochemical function. Iridium in the heterogenite-2H structure is octahedrally coordinated by oxygen. The crystal field splits Ir 5d states into states with t_{2g} and e_g symmetry, opening a gap between them (see Figure 3A). Tetrahedral distortion introduces further t_{2g} degeneracy, but density function theory (DFT) calculations predict that these distortions do not close the band gap (Figure 3B). The width of the calculated band gap is 1.3 eV, which is in fair agreement with the 1.9 eV from analysis of diffuse UV-Vis reflectance (Figure S16), as our DFT method underestimates the magnitude of the gap.[41] IrOOH is therefore be expected to be a semiconductor.

Another tool to probe the crystal field splitting is X-ray absorption spectroscopy (XAS) and we will use O K-edge spectroscopy to do so. At first sight, it does not appear valid to probe the crystal field splitting of the metal center via oxygen, but it is in the case of IrOOH. Oxygen and iridium in IrOOH are strongly hybridized, so that the oxygen partial density of states (PDOS) contains information about the metal center and vice versa (see Figure 2B and S24).

In $Ir^{III}OOH$, iridium has an electron configuration of $[Xe]6s^05d^6$ (Figure 3A) and t_{2g}-like states are fully occupied, leaving only excitations into e_g-like states. The calculated O K-edge spectrum has one main absorption peak at about 534 eV (Figure 3C). However, the experimental O K-edge (shown besides the prediction in Figure 3C) shows a second contribution at lower excitation energies, indicating excitations into the lower-lying t_{2g}-like states. For this to be true, the average oxidation state of iridium must be larger than +3 (Figure 3A).
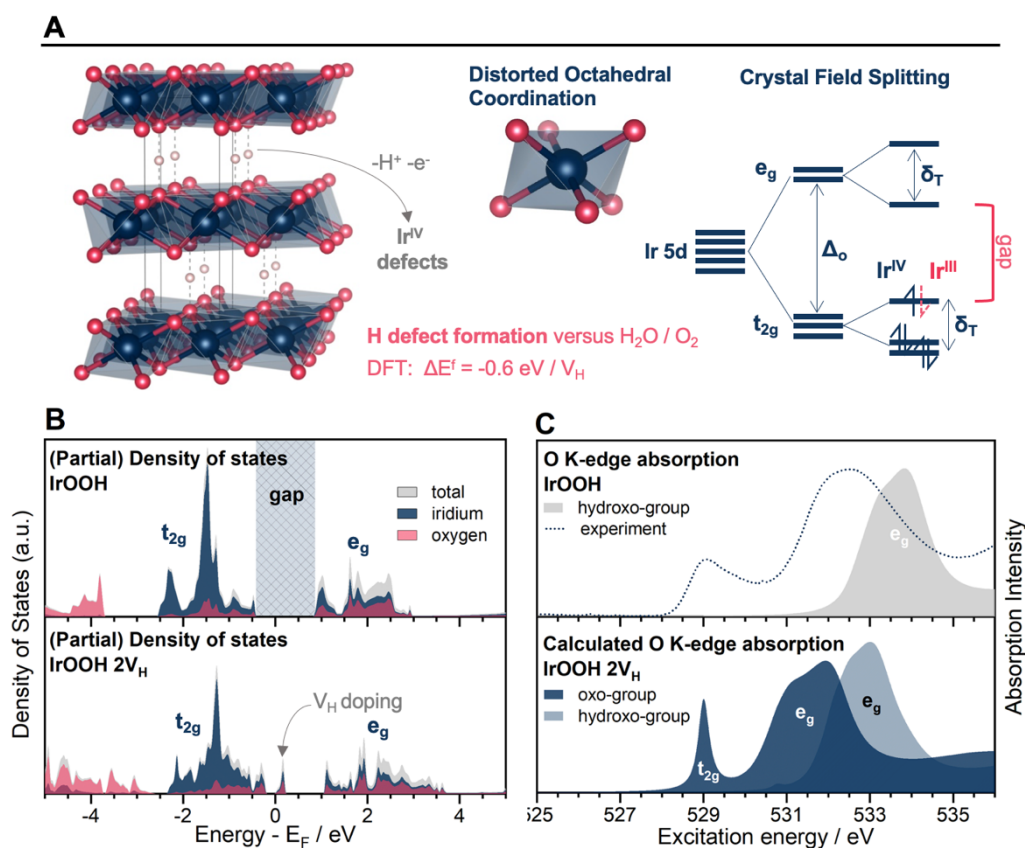

Figure 3: **A** representation of the heterogenite-2*H* crystal structure and a qualitative scheme of the expected crystal field splitting for the valence states of iridium; dark blue, red, and light pink spheres denote Ir, O, and H atoms, respectively; the crystal field splitting is caused by octahedral coordination with O, which splits the Ir 5d states into states with t_{2g} and e_g symmetry, tetragonal distortion further splits these states, the e_g being affected more strongly; **B** total and partial density of states (PDOS) relative to the Fermi-energy of heterogenite-2*H* IrOOH and a version thereof with one hydrogen vacancy in each layer ($2V_H$), resulting in the sum formula $IrO_{1.25}OH_{0.75}$; **C** the respective O K-edge spectra calculated by DFT coupled with the solution of the Bethe-Salpeter equation; the experimental O K-edge absorption of bulk IrOOH is shown as a dotted line.

This deviation from the formal oxidation of +3 can be caused by hydrogen defects, or Ir^{IV} defects (equivalent). To test if these defects are thermodynamically feasible, we introduced hydrogen vacancies

V_H in the ab initio model (Figure 3A). The first two vacancies indeed lowered the formation energy against a reservoir of water and oxygen stepwise, by -0.64 eV each (Table S3). The hydrogen vacancies act as dopants and create states within the gap (see Figure 3B). Excitations into these states from the O 1s core level show up as a white line at 529 eV (see SI for energy calibration), matching the experimental O K-edge spectrum (Figure 3C) and further supporting the hypothesis of hydrogen or Ir^{IV} defects.

To quantify how many hydrogen atoms are missing in between the layers, we used XAS and temperature programmed redution (TPR). Accounting for the possibly undefined hydrogen content, we introduce the general stoichiometry $IrO_{2-2x}(OH)_{2x}$, with x ranging between 0 and 1. For XAS, the integrated white line intensity (WLI) scales with the empty PDOS of the probed element,[42] i.e. the hole character, or oxidation state. The Ir $L_{2,3}$-edge WLI indicated an iridium oxidation state of +3.2, or $IrO_{1.2}(OH)_{0.8}$, (see Figures S18-20) and the O K-edge WLI indicated an oxidation state of +3.7 or $IrO_{1.7}(OH)_{0.3}$ (discussion of Figure S17). For TPR, the initial weight and the amount of consumed hydrogen was used to determine an oxidation state of +3.5, or $IrO_{1.5}(OH)_{0.5}$ (see Figures S11-12). In other words, every fifth to two-out-of-three hydrogens is IrOOH is missing. This variation originates from uncertainty in the methods (see SI) and uncontrolled exposure to air. For simplicity, we will refer to IrOOH with missing hydrogen atoms as $IrO_{1.5}(OH)_{0.5}$, as obtained by TPR. These defects affect the interlayer spacing, the octahedra volume, and octahedra distortion (see Figure S23).

Now that the atomic and electronic structure of $IrO_{1.5}(OH)_{0.5}$ is well characterized by experiments and is fully captured by the ab initio model, we will next evaluate the links between the Ir–O connectivity and electrochemical properties of IrOOH with ab initio methods. To avoid transport limitations and increase interfacial surface area, we will focus on IrOOH nanosheets.

Relationship between connectivity and electrochemical properties

We start with the horizon of expectation for Ir–O speciation, spectroscopy, and electrochemistry by using ab initio calculations. The DFT calculations (see Experimental Section and SI for computational details) were initiated with the crystal structure from SAED and relaxed within the experimental bounds with respect to total energy and forces. The resulting Ir—Ir distance of 3.25 Å (see Table S4) is larger than the 3.15 Å from SAED, which is a well-know shortcoming of the generalized gradient approximation we use.[43,44] The basal plane is entirely made up of what we are going to call trivalent pyramidal oxygen species, or $\mu_{3\Delta}$–O, which are chemically distinct from μ_3–O in rutile type IrO_2 (see SI for hydrogen adsorption calculations). The placement of hydrogen on the basal planes was evaluated on continuous sheets. A structure with symmetric and parallel rows of hydrogen had the lowest energy (see SI). The same structure was terminated perpendicular to the (100) direction to arrive at the edge model with a 1:1 ratio between terminal oxygen (μ_1-O) and bridging oxygen (μ_2-O) (Figure 4).
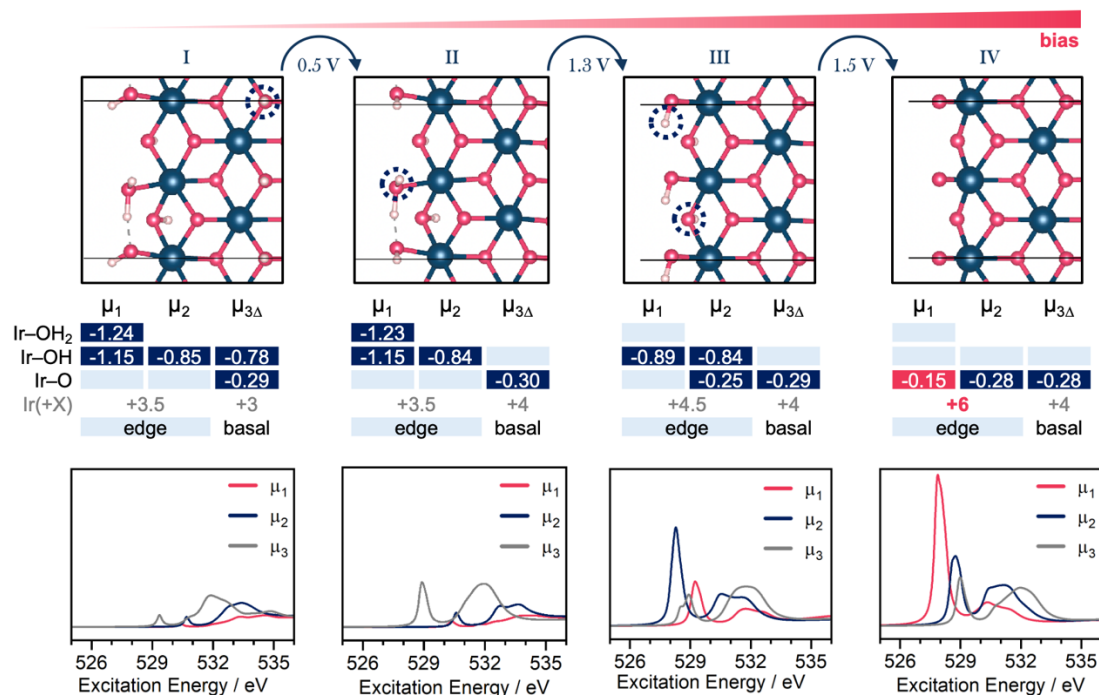
Figure 4: The top shows crystal structure renderings of the most stable IrOOH nanosheet edge structures at a given potential; the potential at which one structure is expected to transition to the other is indicated above them, they are given in Volt against a computational hydrogen electrode; the 3x3 tables in the middle row mark the state of hydrogenation of the oxygens bound to one (μ_1), two (μ_2) and three ($\mu_{3\Delta}$) iridium atoms; the values within these dark blue fields indicate the respective charges on oxygen from a Löwdin population analysis with no normalization; the formal oxidation state of iridium in the basal plane and at the edges is given below the tables; the oxidation states +5 and +6 are marked in red because they are expected to fall into a negative charge transfer regime in which the holes on iridium are strongly shared with neighboring oxygens; the calculated O K-edges averaged for μ_1, μ_2, and μ_3 are shown on the bottom (see Figure S32 for all spectra), the white line intensity is more intense the more hole character resides on the respective oxygen species.

With the model at hand, we first evaluate how nanosheet's protonation changes with bias. Each μ_x–O species exists in a protonated form, i.e. μ_x–OH, and can shed the proton in a proton-coupled electron transfer (PCET), as in μ_x–OH $\rightarrow$ μ_x–O + e$^-$ + H$^+$. The nanosheet can be reduced or oxidized via these PCETs. To predict (de-)protonation potentials, we compared the thermodynamic stability of twelve edge structures with various amounts of hydrogen against a computational electrode (Figure S30). The following phase transitions occur: Deprotonation of $\mu_{3\Delta}$-OH at 0.5 V_{SHE}, deprotonation of μ_1-OH$_2$ and μ_2-OH at 1.3 V_{SHE}, and deprotonation of μ_1-OH at 1.6 V_{SHE} (see Figure 4, structures II & III). Assuming an oxidation state of -2 for oxygen and +1 for hydrogen allows determination of the formal oxidation states of iridium, which equates to successive oxidation from +3, to +4, to +4.5, and +6 (tabulated in middle of Figure 4). Beyond +4, IOHs enter a negative charge transfer regime and electron holes increasingly reside on oxygen.[32,33,35]

This hole character on oxygen is known to play a crucial role for the reactivity of IOHs in the OER. We measured this hole character via the Löwdin charges on oxygen (tables within Figure 4) and the O K-edge WLI, which scales with the empty oxygen PDOS of the probed element.[42] Two trends are observed in the bottom of Figure 4: first, the absorption white line position shifts to lower values with a lower valency, and second, the absorption intensity increases with increasing 2p hole character on oxygen.

When fully deprotonated, the absorption intensity and Löwdin charge of μ_1–O are distinct from the μ_2–O and μ_3–O counterparts, which have nearly equal 2p hole character. As shown in earlier studies,[20,25,26,36] this extensive hole character on μ_1–O leads to radical character and a high reactivity in O–O coupling.
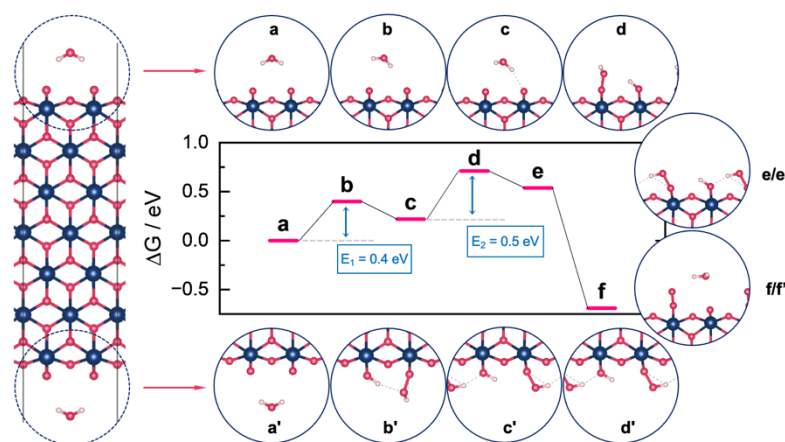

Figure 5: Calculated free energies of the reaction path for water oxidation on μ_1–O referenced to the initial state **a**, the sheet calculations have two sites, on the top and bottom edge, while the latter is marked with an apostroph; since they did not react simultaneously, the structure of the edges are shown separately for a-d and g-h, for e-f and i-j the top edge is representative for both edges (see right hand side); the activation energies for O–O coupling is 0.4 eV for the bottom edge and 0.5 eV for the top edge ($E_{1,2}$, a-e), the subsequent O_2 release (E_3, f-j) is 0.7 eV for the bottom edge with an empty μ_1–O site, and appears barrierless on the top edge, where the transition state was not observed.

To verify that the reaction on μ_1–O is feasible, we calculated the reaction barrier on a μ_1–O site on the edge of an IrOOH nanosheet wth two edges using the climbing image nudged elastic band method (Figure 5).[45] We consider O–O coupling as the rate determining step (detailed discussion in the SI) and found activation energies for between 0.4 and 0.5 eV. These barriers are low compared to the 0.6 eV in Ping et al. on $IrO_2(110)$ using implicit solvation [46] and is expected to be lowered further using explicit solvation.[36] Similarly to studies on $IrO_2(110)$,[36,46] O–O coupling on IrOOH edges includes a proton-transfer to a neighboring μ_1–O site, which makes the reaction a non-concerted electron transfer, or chemical reaction step.

To summarize the expectation from ab initio calculations, we can put on record that there are three disitinct oxygen species on IrOOH nanosheets: μ_1–O, μ_2–O, and $\mu_{3\Delta}$–O, in the order of increasing connectivity. μ_1–O is distinct in that it is an oxyl that is highly reactive in O–O coupling. μ_2–O and $\mu_{3\Delta}$–O have similar hole character, but due to their different connectivity, they have distinct chemistry: The basal plane $\mu_{3\Delta}$–OH deprotonates at a lower potential than μ_2–OH. The O K-edge white line positions of these three surface oxygen species are separated by more than 0.2 eV, which is larger than typical experimental resolution. Knowing the spectroscopic fingerprint, we can now test the relationship between oxygen connectivity and electrochemical behavior with operando X-ray spectroscopy.

Connecting oxygen species to electrochemical currents

The samples for operando X-ray spectroscopy were made from a PEM (FAD by fumatech), the nanosheets, and a graphene blanket (see Figure 6; more information is available in the SI). This arrangement is in contact with bulk electrolyte in which the counter and reference electrode are immersed. Liquid electrolyte (including sulfate ions and protons) can pass through the FAD membrane and form a thin electrolyte layer between the membrane and the working electrode (Figure 6A).[47] This setup allows surface sensitive X-ray spectroscopy at a biased solid-liquid interface using a near-ambient pressure X-ray photoelectron spectroscopy (NAP-XPS) setup. A sample architecture consisting of an FAD membrane, IrOOH nanosheets, and a single layer of graphene (SLG), which is in contact to 0.1 M H_2SO_4, will be referred to as (0.1 M H_2SO_4)/FAD/IrOOH-ns/SLG in the following.
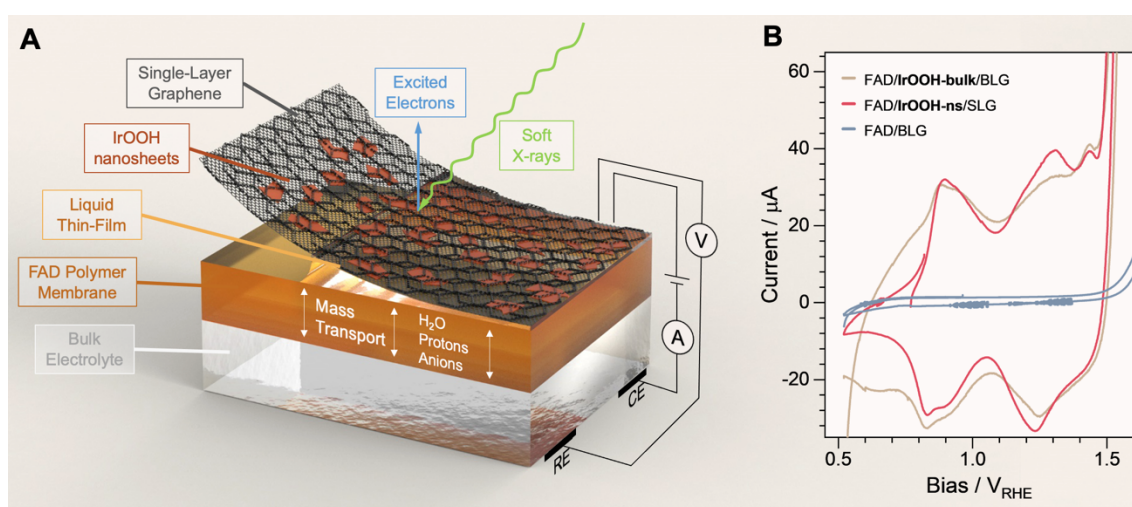

Figure 6: **A** Artistic rendering of the operando samples, comprising the bulk electrolyte (bottom) in which the Ag/AgCl reference electrode and the Pt counter electrode are immersed (bottom right), the FAD polymer membrane through which water, protons, and anions can pass (sandwiched orange layer), and the graphene double layer (BLG, black) with attached IrOOH nanosheets (red platelets); the top is facing vacuum but the evaporation barrier of graphene leads to a liquid thin film between graphene and the polymer mebrane; X-ray spectroscopy is measured from the top using soft X-rays (green arrow); electrons (blue arrow) are detected with a differentially pumped NAP-XPS system. **B** Cyclic voltammetry at 10 mV/s of FAD/BLG without catalyst (blue) and with IrOOH catalyst (beige for dropcasted IrOOH powder, and red for IrOOH nanosheets.

Cyclic voltagrams (CVs) of bulk IrOOH and IrOOH nanosheets are the first test. Both CVs have oxidation features at 0.9 V_{RHE}, 1.3 V_{RHE}, and at 1.4 V_{RHE}, that mostly differ in their width. The delayed reduction of bulk IrOOH below 0.9 V_{RHE} might originate from mass transport limitations. As in the prediction, the three oxidation events separate four phases with the difference that deprotonation of μ_3-OH was predicted 0.4 V earlier than in the experiment, which will be discussed later in the text. In the following, we will investigate each redox transition by operando spectroscopy.

The first transition occurs at about 0.9 V_{RHE} and is predicted to be the transition from a semiconducting (Ir^{III}) to a conducting state (Ir^{IV}). The CV (Figure 6B) switches from a tapered shape to a broader capacitance region, typical for metal-insulator transitions.[48,49] Figure 7B&C show the spectroscopic measurements at 0.5 V_{RHE} in a well-equilibrated state, i.e. at negligible currents (Figure S42). The Ir 4f

spectrum shows two symmetric peaks with a spin doublet separation of 3.0 eV, the expected intensity ratio of 4:3, and a Ir 4f 7/2 peak position of 62.0 eV (see Table S8). Noticeable is the reverse core level shift in comparison with rutile-type IrO_2 appearing at 61.8 eV.[15,50] The O K-edge at 0.5 V_{RHE} (Figure 7B) shows a single contribution at 531.5 eV, which originates from an excitation from the core level into unoccupied e_g-like states (Figure 7A) and is in line with prediction (Figure 4, structure I).
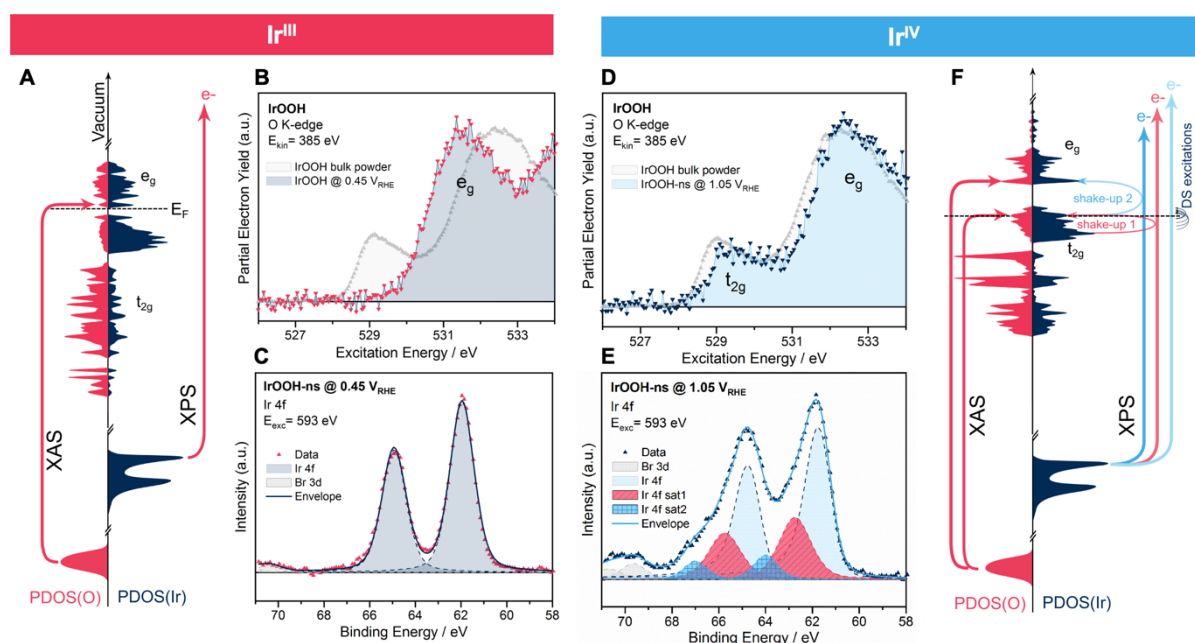

Figure 7: Operando **B & D** O K-edge absorption spectroscopy (XAS) measured in a partial electron yield normalized to the maximum e_g intensity and **C & E** operando Ir 4f X-ray Photoelectron Spectroscopy (XPS) of (0.05 M H_2SO_4)/FAD/IrOOH-ns/SLG at a potential of **B & C** 0.5 V_{RHE} and **D & E** 1.1 V_{RHE}; the excitation schematics for X-ray spectroscopy on sheets of $Ir^{III}OOH$ and $Ir^{IV}OO$ are given in part **A** and **F** of the figure; absorption at 532 eV originates from excitations from O 1s into unoccupied states with e_g symmetry, while the white line at 529 eV originates from an excitation into unoccupied states with t_{2g} symmetry (left part of **A** and **F**); the photoelectrons in XPS experience energy losses from co-excitations from occupied t_2- into unoccupied t_{2g}- and e_g-like states, resulting in an asymmetric Doniach-Ŝunjić line shape (light blue), and two shake-up satellites (red and intense blue); a Shirley-type background was subtracted from the shown Ir 4f XP spectra.

At 1.1 V_{RHE}, the Ir 4f spectrum is clearly asymmetric towards higher binding energies (Figure 7E). Similar to previous work,[15] we fitted using an asymmetric Doniach-Ŝunjić line shape[51] with two shake-up satellites (see Table S8). The BE of the Ir 4f 7/2 is 61.7 eV and the spin doublet separation is 3.0 eV. Fits of the first shake up satellite (Table S8) show an energy loss of ~1 eV, which matches the difference between the Fermi energy and a sharp feature in the occupied PDOS (Figure 7F and S28). The second satellite (sat2 in Table S8) resides ~2 eV above the main line, which matches an excitation from the Fermi energy into a peak in the density of states at 2 eV above the Fermi energy (Figure 7F and S28). The experimental O K-edge has a clear absorption white line slightly above 529 eV and a second broader feature at 532.5 eV (Figure 7D). The spectrum agrees well with what is expected from calculations (Figure 4, structure II).

The IrOO(H) nanosheets reach the state of ~Ir^{IV} at 1.1 V_{RHE} and the basal planes are deprotonated, but the remaining μ_2-OH_x and μ_1-OH_x edge can still be oxidized. The respective PCETs are predicted to

occur at 1.3 V_{RHE} and 1.5 V_{RHE}, as observed in the CVs of IrOOH-ns (Figure 6B). At 1.3 V_{RHE}, deprotonation of μ_2-OH and μ_1-OH$_2$ sites leads to a formal oxidation state of Ir$^{+4.5}$ (Figure 4 structure III) and additional deprotonation of μ_1-OH leads to formally Ir^{VI} (Figure 4 structure IV).

Experimental O K-edge spectra of nanosheets at the OER onset (1.4 V_{RHE}) and under operation conditions (1.6 V_{RHE}) are shown in Figure 8A. At the onset of the OER, μ_2-O contributes at ~528.7 eV and the corresponding Ir 4f spectrum is further broadened (Figure S46). During OER, the O K-edge shifts further towards lower E_{exc}. These changes are qualitative, because the spectra were recorded at different measurement positions to avoid beam damage and thus had to be normalized for comparison (see caption of Figure 7&8). Quantification could be obtained for a given species and measurement position with potentiodynamic X-ray absorption, for which the white line intensity was tracked over multiple potential steps (Figure 8C) and positions. The statistical result is shown in Figure 8D. The signal intensity at 529 eV contains contributions from μ_2-O and μ_1-O, increases with the first oxidation wave at 1.2 V_{RHE}, and saturates approaching OER. The signal at 528 eV captures the resonance characteristic for μ_1-O (see Figure 4). It keeps increasing into the OER, suggesting an active role of oxyl in the reaction.
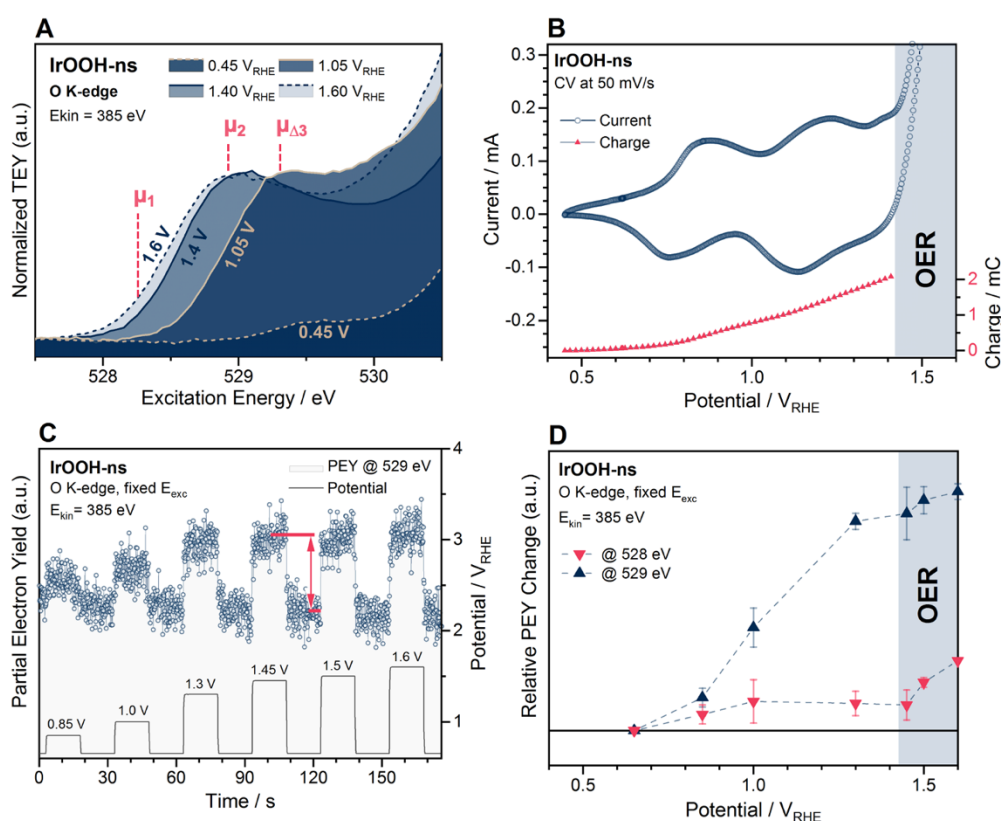

Figure 8: Electrochemical operando spectroscopy of 0.05 M H$_2$SO$_4$/FAD/IrOOH-ns/SLG; **A** O K-edge absorption spectra normalized to the peak intensity of the white line (except at 0.45 V_{RHE}); **B** cyclic voltammogram and the respective integrated charge up to the onset of the OER; **C** exemplary potentiodynamic X-ray absorption showing the applied potential on the bottom (right axis) and the response of the partial electron yield signal at E_{exc}=529 eV (left axis); **D** signal difference relative to the signal intensity at 0.65 V_{RHE}, as indicated in red in part **C**; the signal at 528 eV and 529 eV in **D** is an average from data of four measurement positions; a tail of the 528 eV white line is captured at 529 eV.

Operando spectroscopy confirmed that μ_x–O deprotonation potential decreases with connectivity. It also confirmed the metal insulator transition from formally Ir^{III} to Ir^{IV} via deprotonation of the basal plane $\mu_{3\Delta}$–O. Both μ_2–O and $\mu_{3\Delta}$–O are stable well below OER potentials, but with deprotonation of μ_1–O oxygen starts evolving, as predicted by the strong hole character on μ_1–O. Having linked the model with its electrochemical properties via ab initio methods and operando experiments, we now compare to other IOHs to be able to draw more general trends on how connectivity is linked to performance in the discussion.

Comparisons between IOHs

As a comparison to IrOOH (nanosheets), we use well-studied IOH examples, an amorphous IOH powder from Alfa Aesar (AA-IrO_x) with elements of crystalline hollandite-type and rutile-type phases,[7,15,23,24] calcined rutile-type IrO_2 powder, and anodized Ir nanoparticles (Ir NPs) as in [25]. For Ir NPs, we expect the formation of anodic IOHs with an amorphous and hydrated structure.[52] The electrochemical behavior of the powdered materials was tested on a rotating disk electrode (Figure 9, see SI for details).

The mass activity (Figure 9B) is similar for IrOOH and AA-IrO_x but when normalized to Brunauer-Emmett-Teller (BET) surface area (see Figure 9B and SI) IrOOH shows a much larger intrinsic activity. The activity per surface area of crystalline IrO_2 is comparable to AA-IrOx. The same trend is obtained when normalizing to electrochemical surface area, i.e. capacitance (see Figure S39).

The amorphous AA-IrO_x has a first oxidation feature at 0.45 V_{RHE} and the CV is wider than IrOOH (Figure 9A). Calcined IrO_2 has fewer oxidation features and a large capacitant region (Figure S38). An analysis of the capacitance when oxidized (see Table S6) yielded 26 mF/cm^2 for AA-IrO_x, 4 mF/cm^2 for IrOOH, and 0.5 mF/cm^2 for IrO_2. The last oxidation feature before OER at 1.4 V appears similar in IrOOH and AA-IrO_x but is shifted to 1.6 V_{RHE} for IrO_2.

Assuming octahedral coordination and the limited Ir–O speciation, the electrochemical differences suggest that the varying connectivity influences deprotonation potentials of Ir–O species and their reactivity.
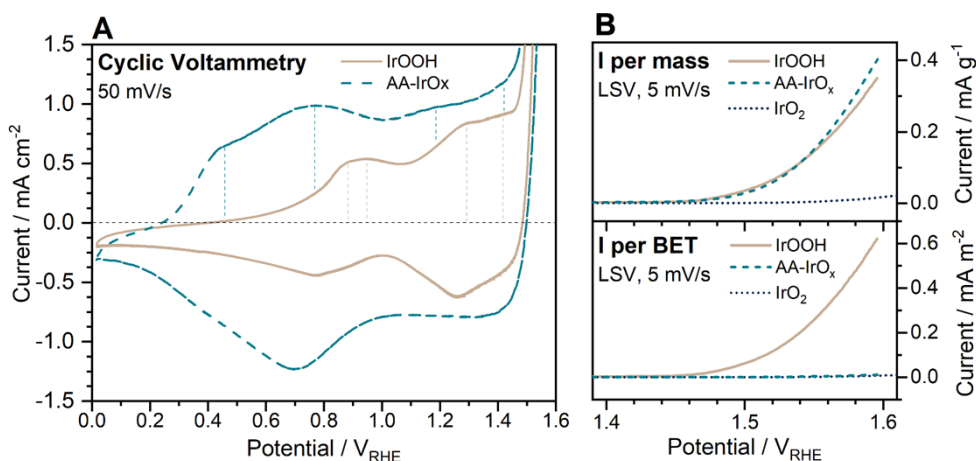
Figure 9: Electrochemistry in Ar-saturated 0.1 M H₂SO₄ of a polished glassy carbon rotating disk coated with a catalyst layer containing Nafion; **A** Cyclic voltammetry of AA-IrOx and IrOOH and **B** their respective linear sweep voltammetry in comparison to rutile type IrO₂; normalization to mass is given on the top, normalization to the BET surface area on the bottom.

Another consequence of varying connectivity is a larger variation in bond strengths. We do a bond strength analysis with peak reduction temperature of TPR in H₂. The molar flow of H₂ at the outlet during a heating ramp from room temperature to 300 °C is given in Figure 10A. The peak reduction event of the roughly 25 mg of powder is finished at 90 °C for AA-IrOₓ, 170 °C for IrOOH, and 215 °C for IrO₂, as summarized in Figure 10B. The two reduction events of AA-IrOx (dash-dot curve in Figure 10A) at room temperature and 75 °C are exothermic, causing a non-linear temperature ramp (see Figure S13) and loop functions (Figure 10A). A similar effect is observed in IrOOH, but less pronounced (Figure S13). The peak reduction temperatures can be used, in first approximation, as a measure of bond strength. A Redhead type analysis of first order gave a Ir–O bond strength of 1.44 eV for IrO₂ and 1.33 eV for IrOOH using the programmed heating rate of 6 K/min.[53] For the strongly exothermic reaction on AA-IrOₓ we used the measured heating rate at peak reduction of 58 K/min, which gives 1.06 eV for the Ir–O bond strength. This analysis shows that a larger distribution of bond strenghts, i.e. lower connectivities, leads to a lower temperature of disintegration. As OER dissolution studies found the same trend,[17–20] Ir–O bond strength seems to relate with oxidative stability. However, the inverse behavior of oxidative dissolution and bond strength raises the question if connectivity mostly influences stability via bond strength distribution, or also via the IOHs electrochemical ability to reduce or oxidize via PCETs.

We investigated the effect of the bias on electrochemical reducibility (Figure 10C-E) and oxidizability (Figure 11) with operando spectroscopy at extreme potentials (0.5 and 1.65 V_RHE). The electrochemical reducibility is measured by the relative WLI between 527 and 530.5 eV stepping from 1.65 V_RHE to 0.5 V_RHE. The WL spectra and the resulting values are given in Figure 10C&D and 12E, respectively. The calcined bulk IrO₂ is not reducible, as expected from single crystal studies.[54] It is followed by AA-IrOx, which is known to have crystalline domains of rutile-type and hollandite-type phases,[7,15,23,24] and

anodized iridium nanoparticles. Dissolution studies also concluded that more amorphous oxides have more absolute dissolution. IrOOH is an outlier in this respect as it is is highly crystalline and reducible.
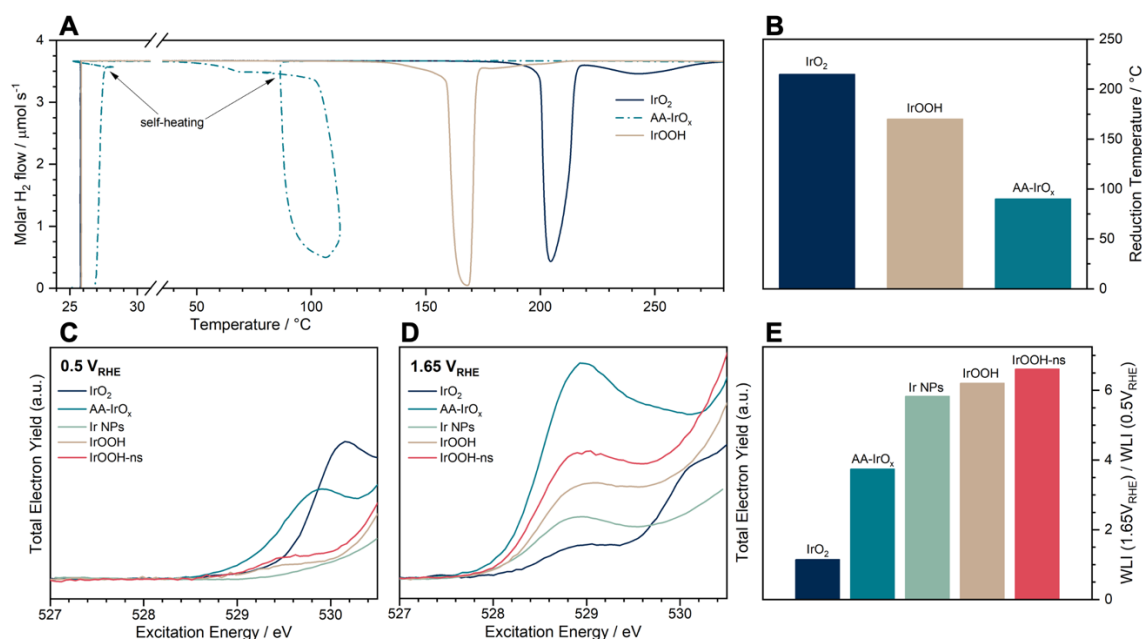

Figure 10: **A** Temperature programmed reduction (TPR) in a flow-through reactor; the measured molar flow of hydrogen downstream of the reactor is shown during a linear heating ramp from room temperature to 300 °C at 6 K/min; reactor inflow at 100 mL/min and 5.0 % hydrogen in argon is 3.7 µmol/s; **B** temperature at which peak reduction has finished, marked by a sharp increase of downstream hydrogen content; **C & D** operando O K-edge white lines normalized to the edge jump at 550 eV, i.e. all oxygen species, at 0.5 V_{RHE} & 1.65 V_{RHE}, respectively; **E** ratio of the white line intensity (WLI) at 1.65 V_{RHE} and 0.5 V_{RHE} integrated between 527 and 530.5 eV, showing the relative reducibility of all oxygen species.

Electrochemical oxidizability is gauged with the average hole character on oxygen at 1.65 V_{RHE}. To obtain this measure, we first normalize to all the integrated absorption intensity between 527 and 530.5 eV – carbonaceous oxygen species and water are not expected to contribute much intensity in this window [25] – and then evaluate the average excitation energy weighted by the absorption intensity. The average hole character increases in the order of IrO_2 < IrOOH ≈ IrOOH-ns < Ir NPs < AA-IrO_x, with AA-IrO_x being the most oxidized on average. Similarly, the respective Ir 4f spectra (Figure S46) become increasingly asymmetric in the order IrO_2 < AA-IrO_x < Ir NPs < IrOOH ≈ IrOOH-ns, suggesting highly oxidized sites in IrOOH, AA-IrO_x and Ir NPs. This ordering shows that lower connectivity allows for higher average oxidation states.
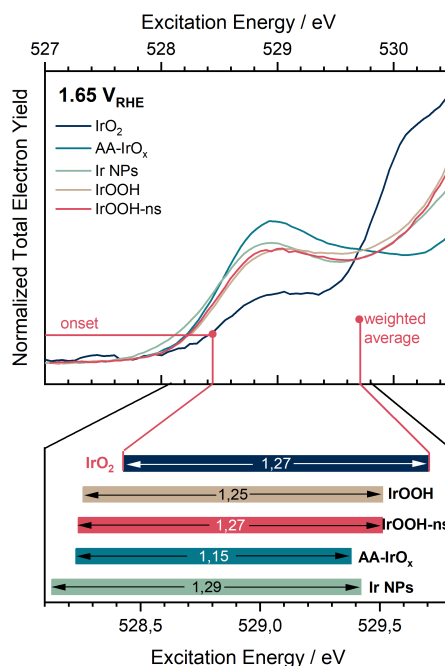
Figure 11: The average and the extreme hole character on oxygen in the OER of different IOHs. **Top** O K-edge white line at 1.65 V_{RHE} with the total intensity between 527 and 530.5 eV normalized to unity; **Bottom** floating bar graph; the average hole character on oxygen marks the right limit of the bars and is the intensity-weighted average excitation energy; the number of oxygen species with extreme hole character was evaluated by the excitation energy at the onset at an intensity of $5.7 \cdot 10^{-3}$ and marks the left limit of the bars; the distance between these marking points, or the length of the bar, is noted at the center of each bar.

If the higher average oxidation states on oxygen explains reactivities, we evaluate the onset of the normalized white lines in Figure 11, a measure of the quantity of μ_1-O oxyl species. When it comes to the number of oxyl species (onset) the order is $IrO_2 <$ IrOOH $\approx$ IrOOH-ns $\approx$ AA-IrO$_x <$ Ir NPs. The span of the bars is similar for all IOHs where one dominant phase is expected, i.e. the crystalline IrOOH and IrO_2. Also the nanoparticles with mixed metallic and amorphous phases have a similar span. The span of the bar is only smaller for AA-IrO$_x$ which is a mixed amorphous and crystalline phase.[24] So we found that IrOOH, AA-IrO$_x$ and Ir NPs during OER have highly oxidized oxygen species that are expected to be active, but the average oxygen in AA-IrO$_x$ and Ir NPs is more oxidized. The onset identifies IrO_2 as the least active (compare Figure 9) but cannot distinguish IrOOH and AA-IrO$_x$. We will return to the meaning of this finding in the discussion.

Final Discussion

This study is intended to narrow the structure gap between atomistic models of iridium oxo-hydroxides (IOHs) and their function as catalysts in acidic water oxidation. Paramount to achieving this goal was to determine the atomic and electronic structure of the model compound IrOOH precisely and evaluate the chemical behavior of interfacial species in comparison to other IOHs. We will first evaluate the success regarding structure, electronic structure, and site chemistry of IrOOH in the following and then move on to more general conclusions about IOHs below.

Atomic structure of IrOOH

The structure was determined using PXRD, PDF, and TEM (Figure 1&2). The results for all structural probes agreed well with ordered, crystalline nanosheets that, when stacked, can best be described by a heterogenite-$2H$ structure. The Ir–O bond lengths and Ir–Ir distances are within 1% before and after exfoliation, chemical etching, or 50 CVs between 0.35 and 1.65 V_{RHE} (Figure 2), indicating structural robustness. IrOOH owes this stability to a dense Ir–O bonding network of trivalent pyramidal $\mu_{3\Delta}$ oxygen species. Unlike typical μ_3–O in rutile-type IrO_2, the $\mu_{3\Delta}$–O in IrOOH exist in a protonated form ($\mu_{3\Delta}$–OH), which allows formal iridium oxidation states of +III throughout the nanosheet. The hydrogen adsorption is in fact 0.67 eV on $\mu_{3\Delta}$–O and 0.21 eV on μ_3–O on a $IrO_2(110)$ surface, based on our DFT calculations. The bulk loses interlayer hydrogen atoms and oxidizes to $\sim IrO_{1.5}(OH)_{0.5}$.

Electronic structure of IrOOH

The electronic structure of IrOOH is expected to be a semiconductor from simple considerations on crystal field splitting, DFT calculations (Figure 3), and evidence from UV-Vis spectroscopy (Figure S16). However, X-ray spectroscopy (Figure 3&S17) and DFT revealed that $IrO_{1.5}(OH)_{0.5}$ is heavily doped with hydrogen vacancies, at the expense of lattice distortion (Figure S23).

If a bias is used to fix the chemical potential of electrons and influence the oxidation state of Ir via PCETs, operando measurement on IrOOH nanosheets (or bulk) agreed well with a gapped $Ir^{III}OOH$ at 0.45 V_{RHE} and a conducting $Ir^{IV}OO$ at 1.05 V_{RHE}.

At 0.45 V_{RHE} we observed a reverse core level shift of Ir 4f (vs IrO_2) and a symmetric line shape. Final state effects are the most likely explanation for these observations. The core hole is screened by ligand charge transfer, leading to symmetric line shapes typical for semiconductors. The binding energy of $Ir^{III}OOH$ is blue shifted compared to the $Ir^{IV}OO$, due to more efficient conduction band screening in $Ir^{IV}OO$. The O K-edge has one broad feature at 532 eV originating from excitations into unoccupied e_g-like states (Figure 3&7A), across the gap, and no white line indicating unoccupied t_{2g}-like states.

At 1.05 V_{RHE} the Ir 4f line becomes asymmetric due to excitations across the fermi level within t_{2g}-like states (Figure 7F) and an O K-edge white line appears at 529 eV. Both are consistent with unoccupied

t_{2g}-like states facilitating conductivity. Support for a metal-insulator transition also comes from the tapered shape of the CVs (Figure 6B) below 0.9 V_{RHE}.

Further oxidation beyond Ir^{IV} pushes the material into a negative charge transfer regime, in which hole character increasingly resides on oxygen instead of iridium.[32,33,35] In response, the O K-edge absorption white line becomes more intense and shifts to lower E_{exc} in calculations and experiment (Figure 4&8 and [20,25]). The respective Ir 4f spectrum is broadened further towards higher BEs (Figure S46), supporting the assertion that iridium centers are further oxidized.[33]

Ir–O speciation in IrOOH and their chemistry

The μ_x–O speciation and their chemistry on IrOOH was tested with TPR, electrochemistry, operando scpectroscopy, and CO titration. We start the discussion with $\mu_{3\Delta}$–O. It has a remarkably low E_{exc} reminiscent of an electron-deficient μ_2–O species active in CO oxidation [15,23] but, unlike the latter, $\mu_{3\Delta}$–O does not oxidize CO at room temperature (Figure S35-37). The Löwdin charges of $\mu_{3\Delta}$–O and μ_2–O are in fact similar. In H_2 TPR, IrOOH reduces at about 170 ˚C (Figure 10), not far from rutile type IrO_2, which reduces at 215 ˚C. The estimated Ir–O bond strengths are 1.4 and 1.3 eV, respectively. Since $IrO_2(110)$ has been shown to have "extraordinary stability" towards cathodic reduction,[54] the similar bond strength of IrOOH at comparable hybridization suggests a good chemical stability of basal plane $\mu_{3\Delta}$–O, i.e. limited cathodic dissolution. The $\mu_{3\Delta}$–OH sites deprotonate in the first redox reaction at about 0.9 V_{RHE} (Figure 4), oxidizing the sheets from +3 to +4.

Further μ_x–O speciation was done with a combination of CVs (Figures 6,8,9), a calculated surface phase diagram (Figure 4&S30), and operando spectroscopy. The PCET of μ_2–O(H) explains the second redox couple at 1.3 V_{RHE}, adding absorption intensity at ~528.7 eV (Figure 4&8). The PCET at μ_1–O(H) explains the third redox couple at 1.45 V_{RHE} (Figure 4&8). The order of the oxidation waves agrees well with other amorphous or crystalline IOHs.[20,25] However, a one-to-one comparison of the transition potentials to calculations is still challenging, due to the influence of surface protonation and solvation in the ab initio model, which has been shown to influence the above energy of PCETs in calculations.[36,46,55] The relatively small unit cell containing two μ_1–O at the edge of the sheet aggravates these influences with respect to the total energy. For example, the $\mu_{3\Delta}$–O below 0.5 V_{SHE} show an absorption white line that is not observed by the operando experiment, suggesting that a dense hydrogen bonding network suppresses the white line originating from non-protonated $\mu_{3\Delta}$–O. Donating hydrogen bonds are in fact known to suppress white line intensity.[25] The lower energy from this solvation could also explain why the deprotonation potential of the basal plane is predicted at 0.5 V_{NHE} (Figure 4) instead of the 0.9 V_{RHE} in experiment (Figure 6,8), though the use of implicit electrolyte is also a likely source of discrepancy; explicit electrolyte increases and broadens the deprotonation window over rutile-type IrO_2.[20,36]

In experiment, the deprotonation of μ_1-OH shows no saturation and increases only with the onset of the OER (Figure 8), suggesting an active role in water oxidation. This stands to reason, since μ_1–O has a Löwdin charge distinct from μ_2–O and μ_3–O (Figure 4) and μ_1–O has been predicted to have radical character on IrO$_2$(110) at formally Ir(+5.33),[25,32] as well as on IrO$_2$(111) and IrO$_2$(001).[33] Iridium at IrOOH nanosheet edges can formally oxidize to +6 (Figure 4) and exhibit an intense white line at low E_{exc} (Figure 4,8&11), both predictive of reactivity in O–O bond formation.[25,33,36] A consequence of μ_1–O being the active site is that the OER takes place at the edges of sheets, not the basal plane. The same was found on ruthenium nanosheets [56] and on cobalt platelets.[57] Since charge storage influences the reaction barrier of O–O coupling,[32,33,35,36] an interesting aspect is that on nanosheets, unlike on bulk materials, the main part of the charge storage would occur on sites that are not directly involved in the reaction.

Summary on IrOOH

Our atomistic model of IrOOH nanosheets connects a wealth of experimental and theoretical findings, a sign of a reliable model. But only the comparison to other IOHs will show if the structure-function relationship of IrOOH nanosheets is exceptional or follows general trends. To find out how far our findings on the IrOOH nanosheets can be generalized, we will compare different IOHs with respect to their thermodynamic stability, their PCET windows, and their OER activity. Figure 12 will serve as a summarizing guide of this discussion.

Thermodynamically stable oxidation states in IOHs

The spontaneous formation of hydrogen defects in bulk IrOOH at ambient conditions (Figure 3) hints at Ir^{III} in the [Xe]6s^{0}5d^6 configuration being metastable or unstable. Along similar lines, a computational study found Ir$_2$O$_3$ being considerably less stable than IrO$_2$, due to relativistic effects.[58] If we then also consider the lack of an experimental proof for an Ir^{III} IOH stable at ambient conditions, it stands to reason that that IOHs thermodynamically favors an oxidation state above +3 in the most stable octahedral coordination,[6,59] unless stabilized by other elements, bias, solvation, or similar. Further reduction of Ir^{III} is expected to be even less stable, due to an additional cost of occupying antibonding e_g-like states.

The upper limit of iridium oxidation state is expected above Ir^{IV}, where IOHs enter the negative charge transfer regime and form electrophilic oxygen species.[32,33,35] The probe molecule CO can identify such species.[23,60] In fact, AA-IrO$_x$ oxidizes CO at room temperature (Figure S34-37 and [23]), pointing towards metastability of those sites in ambient conditions. The active site is most likely μ_2–O, which are known to oxidize CO below formally Ir(+5.33).[23,60] IOHs thus become metastable between +4 and +5.33. The exothermic reaction of CO or H$_2$ at room temperature also point towards metastable domains in AA-IrO$_x$.

As a rule of thumb, IOHs with octahedral coordination and no other elements involved, thermodynamically prefer formal oxidation states between roughly +3.5 and +4.5 (Figure 12) and are metastable or unstable beyond these oxidation states, unless stabilized by solvation or other special circumstances.
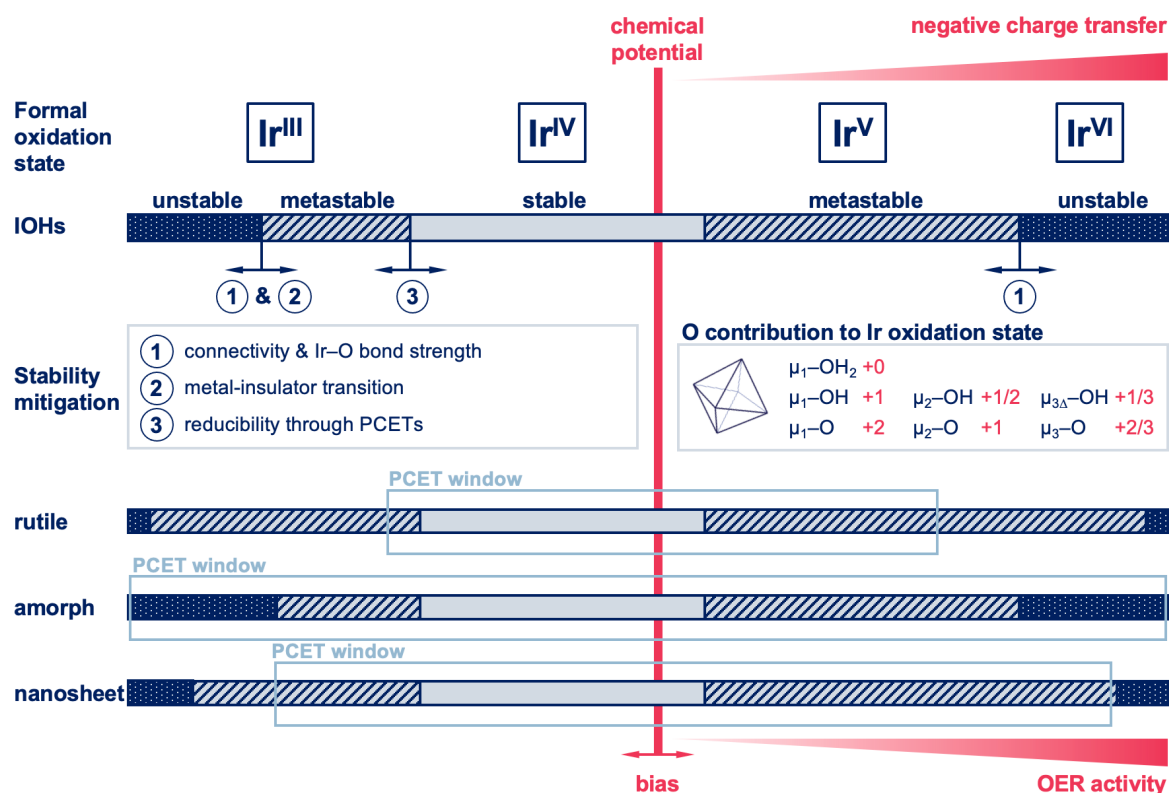

Figure 12: A "cheat-sheet" how activity and stability in IOHs depend on connectivity; the **formal oxidation state** of iridium atoms (oxygen fixed at -2) are given on the top; since iridium is almost always octahedrally coordinated, the formal oxidation state can be calculated from the connectivity of iridium in combination with the protonation state of **octahedrally coordinated oxygens**, as given in the light blue box in the middle right; iridium at the IrOOH edges, for example, are connected to three $\mu_{3\Delta}$, two μ_2, and one μ_1 oxygen species; when these oxygens are fully protonated, the formal oxidation state is $3*1/3 + 2*1/2 + 1*0 = +3$, and when they are fully deprotonated, it is $3*2/3 + 2*1 + 1*2 = +6$; if the coordination is assumed to not change, the connectivity determines the maximum and minimum formal oxidation state that can be reached with **proton-coupled electron transfers (PCETs)**, or electrochemical (de-)protonation, as marked with light blue rectangles in the bottom part; a bias (shown as a red vertical bar) can thus control the formal oxidation state of iridium; since iridium and neighboring oxygens are strongly hybridized, the additional hole character tends to reside increasingly on oxygen beyond Ir(+4) – a **negative charge transfer** regime (red wedge on top) is entered; this leads to increasingly **OER-active oxygen** species (red wedge on bottom); if no bias is applied, formal oxidation states typically return to something between 3.5 and 4.5, marking the **stable region** (light blue of horizontal bars), the bias then either forces the material into a **metastable state** (hatched part of horizontal bars), or, depending on the **bond strength**, into an **unstable state** (dark blue part of horizontal bars); the metastable regime can be extended by the **metal-insulator transition**, alleviating pressure from the bias to reduce, and by the **reducibility** of the structure. Please note that the sharp borders between stable, metastable, and unstable regions indicate trends and are not precisely determined by experiment.

PCET window in IOHs

How far a bias can change the oxidation state without altering the connectivity depends on the PCET window, which we define as the range of oxidation states that can be reached by interfacial species.

Connectivity defines the width of this PCET window because the contribution to the formal oxidation state of (octahedrally coordinated) iridium follows $\mu_1 > \mu_2 > \mu_3$, as shown in the inset of Figure 12. It follows logically that the PCET window is larger for lower connectivities. For example, the prototypical $IrO_2(110)$ surface can reach a minimum oxidation state of +3.33 and a maximum of +5.33, defining the PCET window for a $IrO_2(110)$ model (grey box for crystalline IOHs in Figure 12). In comparison, a highly amorphous material with more μ_2-O(H) and μ_1-O(H) sites is expected to have a much larger PCET window that accommodates a wider variety of oxidation states (Figure 12). In effect, various IOHs showed similar electronic structures at moderate biases between ~0.5 and 1.4 V_{RHE}, despite expected differences in their connectivity. Find the equivalent of Figure 7 for other IOHs in Figure S43-45 and for Figure 8A in Figure S46. However, the acidity of the surface sites, the oxidation states accessible via PCETs influence redox potentials. This is why CVs are sensitive to connectivities.[5,61,62] The comparison of IrOOH and AA-IrO$_x$ (Figure 9), for example, shows that the oxidation from the lowest oxidation state at 0 V_{RHE} and 1.1 V_{RHE} (Ir^{IV}) involves more charge at lower potentials for AA-IrOx. This is consistent with more μ_2 and μ_1 species that allow for lower oxidation states via PCETs (Figure 12). Assignment of redox transitions can be guided by oxygen valence since O–H bond strength and oxidation potential increase with $\mu_1 > \mu_2 > \mu_3$.[25]

In a nutshell, smaller connectivities allow the adaption of a wider range of formal oxidation states through PCETs, i.e. a larger PCET window. The bias foremost controls the oxidation state or electronic structure and, depending on connectivity, the IOHs accommodate this request.

OER activity of IOHs

The barrier of O–O bond formation – the rate determining step of the OER in acids – is known to depend strongly on the hole character on oxygen.[36,46] Three trends increase the hole character on oxygen: first, a smaller valence $\mu_1 > \mu_2 > \mu_3$, second, a larger formal oxidation state on iridium, third the overall hole character at the (sub-)surface.[32,33,35,36] This means that IOHs with lower connectivities have more active sites than their crystalline counterparts and they can be charged far into the negative charge transfer regime (Figure 12). And indeed, the mass activity of AA-IrOx is much higher than that of IrO$_2$ (top Figure 9B).

When it comes to intrinsic activity of the surfaces, IrOOH outperforms both IrO$_2$ and AA-IrOx (bottom Figure 9B). The advantage over IrO$_2$ can be explained clearly with the three trends above. The IrOOH edge sites can oxidize to formal oxidation states of +6, which cannot be reached on typical surfaces of rutile type IrO$_2$.[20,33,63] In addition, the $\mu_{3\Delta}$–O on oxidized IrOOH surfaces have Löwdin charges as large as their μ_2–O counterpart, which are known to influence the rate determining reaction barrier.[36] The comparison between IrOOH and AA-IrO$_x$ is not as straightforward. Both IrOOH and AA-IrO$_x$ have highly oxidized sites which should be equally active (Figure 11). One possible explanation is that the effect of the overall hole character in the (sub-)surface on the reaction barrier works well in a conductive μ_3–O framework [36] but is more localized in amorphous structures due to lower connectivity and

increased disorder.[64] Another is that amorphous oxides have more sites with more hole character on oxygen, but also more sites with lower hole character on oxygen.[65] This wider distribution leads to a less consistent contribution of neighboring hole character to the most active sites, as is the case for IrOOH. A third explanation could be the effectiveness of proton transfer to neighboring sites during O–O bond formation, which might be more scattered in amorphous structures.

In essence, the most active sites are oxyl μ_1–O, a prerequisite for O–O bond formation in acidic OER. A lower connectivity creates more of such active sites, leading to large mass activity. Intrinsic activity of sites seems to also depend on the surroundings of the active sites and is harder to predict.

Electrochemical stability of IOHs

As established above, IOHs are largely thermodynamically unstable below +3.5 and above +4.5. A bias fixes the chemical potential of the electrons and can thus go beyond those limits with PCETs. If this leads to a metastable or unstable state depends on how high the barrier is to break an Ir–O bond. If the bonding framework is weak, the metastable region is narrowed and the structure degrades sooner. The Ir–O bond estimated from the TPR reduction temperature is $IrO_2 > IrOOH > AA\text{-}IrO_x$ (Figure 12). This means IOHs with lower connectivity have a higher number of weak Ir–O bonds and therefore a narrower metastable region (Figure 12). This agrees with large dissolution rates for amorphous IOHs [17–20] and with the finding from Lee et al. that amorphous structures have more weak and more strong bonds.[65] However, thorough dissolution studies on nanosheets are still needed.

The bias should be particularly destructive outside of the PCET window, where the only way to accommodate extreme oxidation states is the breaking of bonds. This delivers an explanation for why – in relative terms – crystalline IrO_2 suffers more from reductive dissolution than from oxidative dissolution when compared to amorphous IOHs.[19,20] The PCET window of IrO_2 does not accommodate oxidation states below +3.33 on the surface and +4 in the bulk, making the material more unstable towards reduction. This is aggravated by the bulk, which is fixed at +4 and stays conductive, and thus cannot reduce the driving force for reduction (as indicated in Figure 12). In absolute terms, amorphous have more reductive and oxidative dissolution, highlighting the dominant rule of connectivity and bond strength.

IrOOH nanosheets combine the best of both worlds. Their $\mu_{3\Delta}$ sites provide large connectivity, which widens the window of metastability, and, unlike their μ_3 counterparts, allow full reduction to a gapped/semiconducting Ir^{III} material, diminishing the destructive effect of reductive potentials.

In summary, the connectivity and bond strength distributions are linked,[65] ultimately leading to correlated activity and stability, as suggested by other authors.[16–18,20] However, the stability of the Ir–O bonding framework appears to be the most important effect for overall dissolution rate, followed by size of the PCET window and reducibility to a gapped/semiconducting state at low potentials.

Conclusion

The present study of IrOOH nanosheets establishes structure-function relationships at the atomic level with a narrow gap between model and experiment. We determined oxyl μ_1–O on the nanosheet edges are the active sites during OER. The intrinsic activity of these nanosheet edge sites is outstanding, even compared to amorphous iridium oxo-hydroxides (IOHs). However, when comparing to other IOHs, IrOOH nanosheets are an outlier in the common trade-off between activity and stability of noble OER catalysts.[16] Their basal plane is a dense framework of trivalent pyramidal $\mu_{3\Delta}$–O that provides both surface electron hole character comparable to $\mu2$–O and a strong bonding network. Nanosheets combine the best of crystalline and amorphous IOHs: they have highly active sites within a stable framework of $\mu_{3\Delta}$–O bonds. A thorough study of nanosheet stability is, however, still missing.

Drawing on a wealth of research on IOHs and the present work, we compiled a set of simple rules to estimate the activity and stability for a given atomic model (depicted also in Figure 12). These simple rules include, but are not limited to:

1. Lower oxygen valence ($\mu_1 > \mu_2 > \mu_3$) increases (A) O-H bond strength, (B) variance of formal iridium oxidation states, and (C) OER activity
2. The formal iridium oxidation state is a good indicator of a site's OER activity
3. The bias foremost controls the oxidation state of the material, which accommodates the request via proton-coupled electron transfers (PCETs)
4. A higher connectivity creates a larger barrier for dissolution
5. IOHs that fully reduce to gapped Ir^{III} diminish destructive effects of reductive potentials

These simple rules are based on many advanced studies, but their application only requires an atomic model and simple bond counting, available to any scientist. The reverse process – from experiment to model – will also be easier with these rules. Simple electrochemistry such as CVs should be sufficient to gain insights into the atomic model of the catalyst.

Outlook

Nanosheets seem to strike the ideal balance between activity and stability with almost complete metal utilization. But despite first signs of long-term stability,[39] more insights into nanosheet dissolution and detachment are needed to make the case for large-scale employment of nanosheets in PEM electrolyzers. Marrying the concept of nanosheets with nanoporous materials, such as hollandite IrO_2,[24,62,65] might increase utilization even further.

We hope that our simple predictive rules will be used, criticized, and refined to empower future studies towards a more complete understanding of OER catalysts. It would be of particular importance to test if the rules extend to other noble metal catalysts and ultimately other transition metal catalysts.

Experimental section

IrOOH powder was obtained from the precursor $K_{0.75}Na_{0.25}IrO_2$ by exchanging alkali cations in 1 M HCl for 5 days. The precursor was synthesized from one equivalent iridium powder, 2.6 equivalent K_2CO_3, and 0.4 equivalent Na_2CO_3, which were heated in air at 850 °C for 120 h. The synthesis follows the procedure of a previous report [66] but the temperature treatment of the precursor was altered in order to avoid a hollandite-type impurity phase (see SI). Exfoliable material was obtained from a precursor synthesized with a different heating procedure, namely 900 ºC for 15 h. Exfoliation was done using tetrabutyl ammonium hydroxide (TBAOH), ultrasonication, and separation by centrifuging the suspensions. Samples for operando specroscopy were produced in a chemical transfer method using FAD membranes by Fumatech (Bietigheim-Bissingen), bilayer- or single-layer graphene (SLG) from Graphenea (San Sebastian), and (dropcasted) catalyst material. The samples were used on an operando cell made of PEEK and held in place by a boron-doped diamond coated niobium lid, as described elsewhere.[47] The obtained nanosheets on free-standing SLG were inspected in a transmission electron microscope (TEM) on a Quantifoil gold grid.

XRD measurements were performed in Bragg-Brentano geometry on a Bruker AXS D8 Advance II theta/theta diffractometer, using Ni filtered Cu Kα_{1+2} radiation. Total scattering measurements were collected using a Stoe Stadi-P diffractometer with AgKα1 radiation, a Ge(111) Johann monochromator, and a DECTRIS Mythen 1K detector in Debye-Scherrer geometry. Their PDF was fitted with simulated PDFs from a structure model based on XRD results using the PDFgui software.

All ab initio density-functional theory (DFT) calculations performed in this work are done with the Quantum EPSRESSO package.[67,68] The generalized gradient approximation is used in form of Perdew-Burke-Ernzerhof (GGA-PBE) type functionals from the Standard Solid State Pseudopotential (SSSP) library [69–72] to treat the exchange and correlation energy. Cutoffs for kinetic energy and charge density are set to 60 Ry and 480 Ry respectively and the Marzari-Vanderbilt type cold smearing was set to a width of 0.01 Ry. A gamma-centered reciprocal grid with an equivalent distance of 0.2 Å^{-1} between adjacent k-points was used throughout the work in order to achieve the k-grid consistency of various structures. The convergence threshold for electronic self-consistency was set to 10^{-8} Ry. Atomic geometries and lattice constants (in-plane lattice constants only in 2D structures) were fixed to the experimental lattice constants (ionic relaxation) and relaxed until the total energy and forces converged within the threshold of 10^{-6} and 10^{-4} atomic units, respectively. The method could lead to slightly compressive strain, since it tends to produce bonds longer than in experiments. In the case of 2D and edge structures, a spacing of at least 18 Å was ensured in the non-periodic directions.

A homebuilt setup was used for flow-through TPR experiments using quartz reactor tubes inside a tube furnace. Gas analysis was done by a thermal conductivity detector, which was calibrated using reference

gas mixtures. Electrochemical measurements (excluding in situ studies) have been done with a rotating disk made of glassy carbon and a thin catalyst coating (40 µg catalyst and ~8 ng Nafion per cm^2).

TEM measurements were conducted using a ThermoFisher Scientific Talos F200X, operated at 200 kV. Special care was taken to minimize beam damage, which was evident from ring-like patterns in the SAEDs after damage.

Ex situ spectroscopy and in situ measurements in CO were both recorded at the BelChem beamline at the BESSY II synchrotron facility. Electrochemical in situ and operando experiments have been done at the ISISS beamline, also at BESSY II. We used Pt wire and an Ag/AgCl electrode as counter and reference electrode, respectively. XAS spectra have been processed with a self-written Python script and XP spectra were fitted using the CasaXPS software.[73] The energy calibration method for O K-edge absorption has an error below ±0.05 eV; the calibration error of XP spectra is below ±0.15 eV and below ±0.1 eV in the case of in situ Ir 4f spectra of IrOOH nanosheets, which were calibrated by second order excitations in situ.

For further information on experimental procedures and methods, please visit the SI.

Acknowledgements

Bibliography

(1)   Holladay, J. D.; Hu, J.; King, D. L.; Wang, Y. An Overview of Hydrogen Production Technologies. *Catal. Today* **2009**, *139* (4), 244–260. https://doi.org/10.1016/j.cattod.2008.08.039.

(2)   Carmo, M.; Fritz, D. L.; Mergel, J.; Stolten, D. A Comprehensive Review on PEM Water Electrolysis. *Int. J. Hydrog. Energy* **2013**, *38*, 4901–4934. https://doi.org/10.1016/j.ijhydene.2013.01.151.

(3)   Buttler, A.; Spliethoff, H. Current Status of Water Electrolysis for Energy Storage, Grid Balancing and Sector Coupling via Power-to-Gas and Power-to-Liquids: A Review. *Renew. Sustain. Energy Rev.* **2018**, *82*, 2440–2454. https://doi.org/10.1016/j.rser.2017.09.003.

(4)   Kibsgaard, J.; Chorkendorff, I. Considerations for the Scaling-up of Water Splitting Catalysts. *Nat. Energy* **2019**, *4* (6), 430–433. https://doi.org/10.1038/s41560-019-0407-1.

(5)   Reier, T.; Teschner, D.; Lunkenbein, T.; Bergmann, A.; Selve, S.; Kraehnert, R.; Schl, R.; Strasser, P. Electrocatalytic Oxygen Evolution on Iridium Oxide : Uncovering Catalyst-Substrate Interactions and Active Iridium Oxide Species. *J. Electrochem. Soc.* **2014**, *161* (9), 876–882. https://doi.org/10.1149/2.0411409jes.

(6)   Abbott, D. F.; Lebedev, D.; Waltar, K.; Povia, M.; Nachtegaal, M.; Fabbri, E.; Copéret, C.; Schmidt, T. J. Iridium Oxide for the Oxygen Evolution Reaction: Correlation between Particle Size, Morphology, and the Surface Hydroxo Layer from Operando XAS. *Chem. Mater.* **2016**, *28*, 6591–6604. https://doi.org/10.1021/acs.chemmater.6b02625.

(7)   Massue, C.; Pfeifer, V.; Huang, X.; Noack, J.; Tarasov, A.; Cap, S.; Schlögl, R. High-Performance Supported Ir-Oxohydroxide Water Oxidation Electrocatalysts. *ChemSusChem* **2017**, 1–16. https://doi.org/10.1002/cssc.201601817.

(8)   Spöri, C.; Briois, P.; Nong, H. N.; Reier, T.; Billard, A.; Kühl, S.; Teschner, D.; Strasser, P. Experimental Activity Descriptors for Iridium-Based Catalysts for the Electrochemical Oxygen Evolution Reaction (OER). *ACS Catal.* **2019**, *9* (8), 6653–6663. https://doi.org/10.1021/acscatal.9b00648.

(9)   Kötz, R.; Neff, H.; Stucki, S. Anodic Iridium Oxide Films: XPS-Studies of Oxidation State Changes And. *J. Electrochem. Soc.* **1984**, *131* (1), 72–77. https://doi.org/10.1149/1.2115548.

(10)   Hall, H. Y.; Sherwood, P. M. A. X-Ray Photoelectron Spectroscopic Studies of the Iridium Electrode System. *J. Chem. Soc., Faraday Trans. 1* **1984**, *80*, 135–152. https://doi.org/10.1039/F19848000135.

(11)   Smith, R. D. L.; Sporinova, B.; Fagan, R. D.; Trudel, S.; Berlinguette, C. P. Facile Photochemical

Preparation of Amorphous Iridium Oxide Films for Water Oxidation Catalysis. *Chem. Mater.* **2014**, *26*, 1654–1659. https://doi.org/10.1021/cm4041715.

(12)   Li, T.; Kasian, O.; Cherevko, S.; Zhang, S.; Geiger, S.; Scheu, C.; Felfer, P.; Raabe, D.; Gault, B.; Mayrhofer, K. J. J. Atomic-Scale Insights into Surface Species of Electrocatalysts in Three Dimensions. *Nat. Catal.* **2018**, *1* (4), 300–305. https://doi.org/10.1038/s41929-018-0043-3.

(13)   Trasatti, S. Electrocatalysis in the Anodic Evolution of Oxygen and Chlorine. *Electrochim. Acta* **1984**, *29* (11), 1503–1512. https://doi.org/10.1016/0013-4686(84)85004-5.

(14)   Bernicke, M.; Ortel, E.; Reier, T.; Bergmann, A.; Ferreira De Araujo, J.; Strasser, P.; Kraehnert, R. Iridium Oxide Coatings with Templated Porosity as Highly Active Oxygen Evolution Catalysts: Structure-Activity Relationships. *ChemSusChem* **2015**, *8* (11), 1908–1915. https://doi.org/10.1002/cssc.201402988.

(15)   Pfeifer, V.; Jones, T. E.; Velasco Vélez, J. J.; Massué, C.; Arrigo, R.; Teschner, D.; Girgsdies, F.; Scherzer, M.; Greiner, M. T.; Allan, J.; et al. The Electronic Structure of Iridium and Its Oxides. *Surf. Interface Anal.* **2016**, *48* (5), 261–273. https://doi.org/10.1002/sia.5895.

(16)   Wei, C.; Wang, Z.; Otani, K.; Hochfilzer, D.; Zhang, K.; Nielsen, R.; Chorkendorff, I.; Kibsgaard, J. Benchmarking Electrocatalyst Stability for Acidic Oxygen Evolution Reaction: The Crucial Role of Dissolved Ion Concentration. *ACS Catal.* **2023**, 14058–14069. https://doi.org/10.1021/acscatal.3c03257.

(17)   Cherevko, S.; Reier, T.; Zeradjanin, A. R.; Pawolek, Z.; Strasser, P.; Mayrhofer, K. J. J. Stability of Nanostructured Iridium Oxide Electrocatalysts during Oxygen Evolution Reaction in Acidic Environment. *Electrochem. commun.* **2014**, *48*, 81–85. https://doi.org/10.1016/j.elecom.2014.08.027.

(18)   Geiger, S.; Kasian, O.; Shrestha, B. R.; Mingers, A. M.; Mayrhofer, K. J. J.; Cherevko, S. Activity and Stability of Electrochemically and Thermally Treated Iridium for the Oxygen Evolution Reaction. *J. Electrochem. Soc.* **2016**, *163* (11), F3132–F3138. https://doi.org/10.1149/2.0181611jes.

(19)   Jovanovič, P.; Hodnik, N.; Ruiz-Zepeda, F.; Arčon, I.; Jozinović, B.; Zorko, M.; Bele, M.; Šala, M.; Šelih, V. S.; Hočevar, S.; et al. Electrochemical Dissolution of Iridium and Iridium Oxide Particles in Acidic Media: Transmission Electron Microscopy, Electrochemical Flow Cell Coupled to Inductively Coupled Plasma Mass Spectrometry, and X-Ray Absorption Spectroscopy Study. *J. Am. Chem. Soc.* **2017**, *139* (36), 12837–12846. https://doi.org/10.1021/jacs.7b08071.

(20)   Mom, R. V; Falling, L. J.; Kasian, O.; Algara-Siller, G.; Teschner, D.; Crabtree, R. H.; Knop-Gericke, A.; Mayrhofer, K. J. J.; Velasco-Vélez, J.-J.; Jones, T. E. Operando Structure–Activity–

Stability Relationship of Iridium Oxides during the Oxygen Evolution Reaction. *ACS Catal.* **2022**, *12* (9), 5174–5184. https://doi.org/10.1021/acscatal.1c05951.

(21)   Over, H. Fundamental Studies of Planar Single-Crystalline Oxide Model Electrodes (RuO2 , IrO2) for Acidic Water Splitting. *ACS Catal.* **2021**, *11* (14), 8848–8871. https://doi.org/10.1021/acscatal.1c01973.

(22)   Yang, Y.; Xiong, Y.; Zeng, R.; Lu, X.; Krumov, M.; Huang, X.; Xu, W.; Wang, H.; Disalvo, F. J.; Brock, J. D.; et al. Operando Methods in Electrocatalysis. *ACS Catal.* **2021**, *11* (3), 1136–1178. https://doi.org/10.1021/acscatal.0c04789.

(23)   Pfeifer, V.; Jones, T. E.; Wrabetz, S.; Massué, C.; Velasco Vélez, J. J.; Arrigo, R.; Scherzer, M.; Piccinin, S.; Hävecker, M.; Knop-Gericke, A.; et al. Reactive Oxygen Species in Iridium-Based OER Catalysts. *Chem. Sci.* **2016**, *7*, 6791–6795. https://doi.org/10.1039/c6sc01860b.

(24)   Willinger, E.; Massué, C.; Schlögl, R.; Willinger, M. G. Identifying Key Structural Features of IrOx Water Splitting Catalysts. *J. Am. Chem. Soc.* **2017**, *139* (34), 12093–12101. https://doi.org/10.1021/jacs.7b07079.

(25)   Frevel, L. J.; Mom, R.; Velasco-Vélez, J.-J.; Plodinec, M.; Knop-Gericke, A.; Schlögl, R.; Jones, T. E. In Situ X-Ray Spectroscopy of the Electrochemical Development of Iridium Nanoparticles in Confined Electrolyte. *J. Phys. Chem. C* **2019**, *123* (14), 9146–9152. https://doi.org/10.1021/acs.jpcc.9b00731.

(26)   Velasco Vélez, J. J.; Bernsmeier, D.; Mom, R. V.; Zeller, P.; Shao-Horn, Y.; Roldan Cuenya, B.; Knop-Gericke, A.; Schlögl, R.; Jones, T. E. Iridium Oxide Coordinatively Unsaturated Active Sites Govern the Electrocatalytic Oxidation of Water. *Adv. Energy Mater.* **2024**, *2303407*, 1–10. https://doi.org/10.1002/aenm.202303407.

(27)   Carbonio, E. A.; Velasco-Velez, J.-J.; Schlögl, R.; Knop-Gericke, A. Perspective—Outlook on Operando Photoelectron and Absorption Spectroscopy to Probe Catalysts at the Solid-Liquid Electrochemical Interface. *J. Electrochem. Soc.* **2020**, *167* (5), 054509. https://doi.org/10.1149/1945-7111/ab68d2.

(28)   Velasco-Vélez, J.-J.; Falling, L. J.; Bernsmeier, D.; Sear, M. J.; Clark, P. C. J.; Chan, T.-S.; Stotz, E.; Hävecker, M.; Kraehnert, R.; Knop-Gericke, A.; et al. A Comparative Study of Electrochemical Cells for in Situ X-Ray Spectroscopies in the Soft and Tender x-Ray Range. *J. Phys. D. Appl. Phys.* **2021**, *54* (12), 124003. https://doi.org/10.1088/1361-6463/abd2ed.

(29)   Sanchez Casalongue, H. G.; Ng, M. L.; Kaya, S.; Friebel, D.; Ogasawara, H.; Nilsson, A. In Situ Observation of Surface Species on Iridium Oxide Nanoparticles during the Oxygen Evolution Reaction. *Angew. Chem., Int. Ed.* **2014**, *53*, 7169–7172. https://doi.org/10.1002/anie.201402311.

(30)　Saveleva, V. A.; Wang, L.; Teschner, D.; Jones, T.; Gago, A. S.; Friedrich, K. A.; Zafeiratos, S.; Schlögl, R.; Savinova, E. R. Operando Evidence for a Universal Oxygen Evolution Mechanism on Thermal and Electrochemical Iridium Oxides. *J. Phys. Chem. Lett.* **2018**, *9* (11), 3154–3160. https://doi.org/10.1021/acs.jpclett.8b00810.

(31)　Pfeifer, V.; Jones, T. E.; Velasco Vélez, J. J.; Arrigo, R.; Piccinin, S.; Hävecker, M.; Knop-Gericke, A.; Schlögl, R. In Situ Observation of Reactive Oxygen Species Forming on Oxygen-Evolving Iridium Surfaces. *Chem. Sci.* **2017**, *8*, 2143–2149. https://doi.org/10.1039/c6sc04622c.

(32)　Velasco-Vélez, J. J.; Jones, T. E.; Streibel, V.; Hävecker, M.; Chuang, C.-H.; Frevel, L.; Plodinec, M.; Centeno, A.; Zurutuza, A.; Wang, R.; et al. Electrochemically Active Ir NPs on Graphene for OER in Acidic Aqueous Electrolyte Investigated by In Situ and Ex Situ Spectroscopies. *Surf. Sci.* **2019**, *681*, 1–8. https://doi.org/10.1016/j.susc.2018.10.021.

(33)　Velasco-Vélez, J. J.; Carbonio, E. A.; Chuang, C. H.; Hsu, C. J.; Lee, J. F.; Arrigo, R.; Hävecker, M.; Wang, R.; Plodinec, M.; Wang, F. R.; et al. Surface Electron-Hole Rich Species Active in the Electrocatalytic Water Oxidation. *J. Am. Chem. Soc.* **2021**, *143* (32), 12524–12534. https://doi.org/10.1021/jacs.1c01655.

(34)　Velasco Vélez, J. J.; Bernsmeier, D.; Jones, T. E.; Zeller, P.; Carbonio, E.; Chuang, C. H.; Falling, L. J.; Streibel, V.; Mom, R. V.; Hammud, A.; et al. The Rise of Electrochemical NAPXPS Operated in the Soft X-Ray Regime Exemplified by the Oxygen Evolution Reaction on IrOx Electrocatalysts. *Faraday Discuss.* **2022**, *236* (1), 103–125. https://doi.org/10.1039/d1fd00114k.

(35)　Nong, H. N.; Reier, T.; Oh, H.-S.; Gliech, M.; Paciok, P.; Vu, T. H. T.; Teschner, D.; Heggen, M.; Petkov, V.; Schlögl, R.; et al. A Unique Oxygen Ligand Environment Facilitates Water Oxidation in Hole-Doped IrNiOx Core–Shell Electrocatalysts. *Nat. Catal.* **2018**, *1* (11), 841–851. https://doi.org/10.1038/s41929-018-0153-y.

(36)　Nong, H. N.; Falling, L. J.; Bergmann, A.; Klingenhof, M.; Tran, H. P.; Spöri, C.; Mom, R.; Timoshenko, J.; Zichittella, G.; Knop-Gericke, A.; et al. Key Role of Chemistry versus Bias in Electrocatalytic Oxygen Evolution. *Nature* **2020**, *587* (7834), 408–413. https://doi.org/10.1038/s41586-020-2908-2.

(37)　Takimoto, D.; Fukuda, K.; Miyasaka, S.; Ishida, T.; Ayato, Y.; Mochizuki, D.; Shimizu, W.; Sugimoto, W. Synthesis and Oxygen Electrocatalysis of Iridium Oxide Nanosheets. *Electrocatalysis* **2017**, *8* (2), 144–150. https://doi.org/10.1007/s12678-016-0348-4.

(38)　Weber, D.; Schoop, L. M.; Wurmbrand, D.; Laha, S.; Podjaski, F.; Duppel, V.; Müller, K.; Starke, U.; Lotsch, B. V. IrOOH Nanosheets as Acid Stable Electrocatalysts for the Oxygen Evolution Reaction. *J. Mater. Chem. A* **2018**, *6* (43), 21558–21566.

https://doi.org/10.1039/C8TA07950A.

(39)   Fan, Z.; Ji, Y.; Shao, Q.; Geng, S.; Zhu, W.; Liu, Y.; Liao, F.; Hu, Z.; Chang, Y. C.; Pao, C. W.; et al. Extraordinary Acidic Oxygen Evolution on New Phase 3R-Iridium Oxide. *Joule* **2021**, *5* (12), 3221–3234. https://doi.org/10.1016/j.joule.2021.10.002.

(40)   Bernt, M.; Siebel, A.; Gasteiger, H. A. Analysis of Voltage Losses in PEM Water Electrolyzers with Low Platinum Group Metal Loadings. *J. Electrochem. Soc.* **2018**, *165* (5), F305–F314. https://doi.org/10.1149/2.0641805jes.

(41)   Cohen, A. J.; Mori-Sánchez, P.; Yang, W. Insights into Current Limitations of Density Functional Theory. *Science* **2008**, *321* (5890), 792–794. https://doi.org/10.1126/science.1158722.

(42)   Stöhr, J.; König, H. Determination of Spin- and Orbital-Moment Anisotropies in Transition Metals by Angle-Dependent X-Ray Magnetic Circular Dichroism. *Phys. Rev. Lett.* **1995**, *75* (20), 3748–3751. https://doi.org/10.1103/PhysRevLett.75.3748.

(43)   Haas, P.; Tran, F.; Blaha, P. Calculation of the Lattice Constant of Solids with Semilocal Functionals. *Phys. Rev. B - Condens. Matter Mater. Phys.* **2009**, *79* (8), 1–10. https://doi.org/10.1103/PhysRevB.79.085104.

(44)   Tran, F.; Stelzl, J.; Blaha, P. Rungs 1 to 4 of DFT Jacob's Ladder: Extensive Test on the Lattice Constant, Bulk Modulus, and Cohesive Energy of Solids. *J. Chem. Phys.* **2016**, *144* (20). https://doi.org/10.1063/1.4948636.

(45)   Henkelman, G.; Uberuaga, B. P.; Jónsson, H. A Climbing Image Nudged Elastic Band Method for Finding Saddle Points and Minimum Energy Paths. *J. Chem. Phys.* **2000**, *113* (22), 9901–9904. https://doi.org/10.1063/1.1329672.

(46)   Ping, Y.; Nielsen, R. J.; Goddard, W. A. The Reaction Mechanism with Free Energy Barriers at Constant Potentials for the Oxygen Evolution Reaction at the IrO 2 (110) Surface. *J. Am. Chem. Soc.* **2017**, *139* (1), 149–155. https://doi.org/10.1021/jacs.6b07557.

(47)   Falling, L. J.; Mom, R. V.; Sandoval Diaz, L. E.; Nakhaie, S.; Stotz, E.; Ivanov, D.; Hävecker, M.; Lunkenbein, T.; Knop-Gericke, A.; Schlögl, R.; et al. Graphene-Capped Liquid Thin Films for Electrochemical Operando X-Ray Spectroscopy and Scanning Electron Microscopy. *ACS Appl. Mater. Interfaces* **2020**, *12* (33), 37680–37692. https://doi.org/10.1021/acsami.0c08379.

(48)   Conway, B. E.; Mozota, J. Surface and Bulk Processes at Oxidized Iridium Electrodes-II. Conductivity-Switched Behaviour of Thick Oxide Films. *Electrochim. Acta* **1983**, *28*, 9–16. https://doi.org/10.1016/0013-4686(83)85080-4.

(49)   Costentin, C.; Porter, T. R.; Savéant, J.-M. Conduction and Reactivity in Heterogeneous-

Molecular Catalysis: New Insights in Water Oxidation Catalysis by Phosphate Cobalt Oxide Films. *J. Am. Chem. Soc.* **2016**, *138* (17), 5615–5622. https://doi.org/10.1021/jacs.6b00737.

(50)   Freakley, S. J.; Ruiz-Esquius, J.; Morgan, D. J. The X-Ray Photoelectron Spectra of Ir, IrO2 and IrCl3 Revisited. *Surf. Interface Anal.* **2017**, *49* (8), 794–799. https://doi.org/10.1002/sia.6225.

(51)   Doniach, S.; Sunjic, M. Many-Electron Singularity in X-Ray Photoemission and X-Ray Line Spectra from Metals. *J. Phys. C Solid State Phys.* **1970**, *3* (2), 285–291. https://doi.org/10.1088/0022-3719/3/2/010.

(52)   Scherzer, M. Grazing Incidence X-Ray Diffraction - Application on Catalyst Surfaces -, TU Berlin, 2018.

(53)   de Jong, A. M.; Niemantsverdriet, J. W. Thermal Desorption Analysis: Comparative Test of Ten Commonly Applied Procedures. *Surf. Sci.* **1990**, *233* (3), 355–365. https://doi.org/10.1016/0039-6028(90)90649-S.

(54)   Weber, T.; Vonk, V.; Abb, M. J. S.; Evertsson, J.; Sandroni, M.; Drnec, J.; Stierle, A.; Lundgren, E.; Over, H. Extraordinary Stability of IrO2(110) Ultrathin Films Supported on TiO2(110) under Cathodic Polarization. *J. Phys. Chem. Lett.* **2020**, *11* (21), 9057–9062. https://doi.org/10.1021/acs.jpclett.0c02730.

(55)   Gauthier, J. A.; Dickens, C. F.; Chen, L. D.; Doyle, A. D.; Nørskov, J. K. Solvation Effects for Oxygen Evolution Reaction Catalysis on IrO2(110). *J. Phys. Chem. C* **2017**, *121*, 11455–11463. https://doi.org/10.1021/acs.jpcc.7b02383.

(56)   Laha, S.; Lee, Y.; Podjaski, F.; Weber, D.; Duppel, V.; Schoop, L. M.; Pielnhofer, F.; Scheurer, C.; Müller, K.; Starke, U.; et al. Ruthenium Oxide Nanosheets for Enhanced Oxygen Evolution Catalysis in Acidic Medium. *Adv. Energy Mater.* **2019**, *6*, 1803795. https://doi.org/10.1002/aenm.201803795.

(57)   Mefford, J. T.; Akbashev, A. R.; Kang, M.; Bentley, C. L.; Gent, W. E.; Deng, H. D.; Alsem, D. H.; Yu, Y. S.; Salmon, N. J.; Shapiro, D. A.; et al. Correlative Operando Microscopy of Oxygen Evolution Electrocatalysts. *Nature* **2021**, *593* (7857), 67–73. https://doi.org/10.1038/s41586-021-03454-x.

(58)   Miao, M.-S.; Seshadri, R. Rh2O3 versus IrO2: Relativistic Effects and the Stability of Ir4+. *J. Phys. Condens. Matter* **2012**, *24* (21), 215503. https://doi.org/10.1088/0953-8984/24/21/215503.

(59)   Clancy, J. P.; Chen, N.; Kim, C. Y.; Chen, W. F.; Plumb, K. W.; Jeon, B. C.; Noh, T. W.; Kim, Y. J. Spin-Orbit Coupling in Iridium-Based 5d Compounds Probed by x-Ray Absorption Spectroscopy. *Phys. Rev. B - Condens. Matter Mater. Phys.* **2012**, *86* (19), 1–8. https://doi.org/10.1103/PhysRevB.86.195131.

(60)   Carbonio, E. A.; Sulzmann, F.; Teschner, D.; Velasco-Vélez, J. J.; Hävecker, M.; Gericke, A. K.; Schlögl, R.; Jones, T. Thermal Synthesis of Electron Deficient Oxygen Species on Crystalline IrO 2. *Catal. Sci. Technol.* **2024**, *14* (3), 572–580. https://doi.org/10.1039/D3CY01026K.

(61)   Ardizzone, S.; Carugati, A.; Trasatti, S. Properties of Thermally Prepared Iridium Dioxide Electrodes. *J. Electroanal. Chem.* **1981**, *126*, 287–292. https://doi.org/10.1016/S0022-0728(81)80437-8.

(62)   Ruiz Esquius, J. Catalysis to Produce Solar Fuels: From the Production of Hydrogen via Water Splitting, to Hydrogen Conversion to Methanol by Its Reaction with CO 2, 2019.

(63)   Opalka, D.; Scheurer, C.; Reuter, K. Ab Initio Thermodynamics Insight into the Structural Evolution of Working IrO2 Catalysts in Proton-Exchange Membrane Electrolyzers. *ACS Catal.* **2019**, *9* (6), 4944–4950. https://doi.org/10.1021/acscatal.9b00796.

(64)   Anderson, P. W. Absence of Diffusion in Certain Random Lattices. *Phys. Rev.* **1958**, *109* (5), 1492–1505. https://doi.org/10.1103/PhysRev.109.1492.

(65)   Lee, S.; Lee, Y. J.; Lee, G.; Soon, A. Activated Chemical Bonds in Nanoporous and Amorphous Iridium Oxides Favor Low Overpotential for Oxygen Evolution Reaction. *Nat. Commun.* **2022**, *13* (1), 1–10. https://doi.org/10.1038/s41467-022-30838-y.

(66)   Weber, D.; Schoop, L. M.; Wurmbrand, D.; Nuss, J.; Seibel, E. M.; Tafti, F. F.; Ji, H.; Cava, R. J.; Dinnebier, R. E.; Lotsch, B. V. Trivalent Iridium Oxides: Layered Triangular Lattice Iridate K0.75 Na0.25 IrO2 and Oxyhydroxide IrOOH. *Chem. Mater.* **2017**, *29*, 8338–8345. https://doi.org/10.1021/acs.chemmater.7b02683.

(67)   Giannozzi, P.; Baroni, S.; Bonini, N.; Calandra, M.; Car, R.; Cavazzoni, C.; Ceresoli, D.; Chiarotti, G. L.; Cococcioni, M.; Dabo, I.; et al. QUANTUM ESPRESSO: A Modular and Open-Source Software Project for Quantum Simulations of Materials. *J. Phys. Condens. Matter* **2009**, *21*, 395502. https://doi.org/10.1088/0953-8984/21/39/395502.

(68)   Giannozzi, P.; Andreussi, O.; Brumme, T.; Bunau, O.; Buongiorno Nardelli, M.; Calandra, M.; Car, R.; Cavazzoni, C.; Ceresoli, D.; Cococcioni, M.; et al. Advanced Capabilities for Materials Modelling with Quantum ESPRESSO. *J. Phys. Condens. Matter* **2017**, *29* (46), 465901. https://doi.org/10.1088/1361-648X/aa8f79.

(69)   Prandini, G.; Marrazzo, A.; Castelli, I. E.; Mounet, N.; Marzari, N. Precision and Efficiency in Solid-State Pseudopotential Calculations. *npj Comput. Mater.* **2018**, *4* (1), 72. https://doi.org/10.1038/s41524-018-0127-2.

(70)   Lejaeghere, K.; Bihlmayer, G.; Bjorkman, T.; Blaha, P.; Blugel, S.; Blum, V.; Caliste, D.; Castelli, I. E.; Clark, S. J.; Dal Corso, A.; et al. Reproducibility in Density Functional Theory

Calculations of Solids. *Science* **2016**, *351* (6280), aad3000. https://doi.org/10.1126/science.aad3000.

(71) Garrity, K. F.; Bennett, J. W.; Rabe, K. M.; Vanderbilt, D. Pseudopotentials for High-Throughput DFT Calculations. *Comput. Mater. Sci.* **2014**, *81*, 446–452. https://doi.org/10.1016/j.commatsci.2013.08.053.

(72) Dal Corso, A. Pseudopotentials Periodic Table: From H to Pu. *Comput. Mater. Sci.* **2014**, *95*, 337–350. https://doi.org/10.1016/j.commatsci.2014.07.043.

(73) Fairley, N.; Carrick, A. CasaXPS. 2017.